Thesis

M.A. ter Wee

Ultrafast ultrasound for super-resolution imaging

The effect of pulse inversion and harmonic- or SVD-filtering on microbubble detection

TU Delft

Thesis

by

M.A. ter Wee

to obtain the degree of Master of Science
at the Delft University of Technology,
to be defended publicly on March 29, 2021 at 4 PM.

Student number: 4956931
Project duration: March 1, 2020 – March 29, 2021
Thesis committee:

Dr. ir. M. Verweij,	TU Delft
Dr. ir. R. Vos,	TU Delft, supervisor
Dr. ir. R. Deckers,	UMC Utrecht, supervisor
Dr. S. Iskander-Rizk,	TU Delft

TU Delft

Abstract

Background/purpose: The mapping of microvasculature requires a high-resolution imaging method. Super-resolution ultrasound-imaging can provide such high resolution by detecting individual microbubbles (MBs) in a flow circuit. This method relies on the dynamic appearance of MBs, which appear as point scatterers on the US image, mixed with tissue signal. The detection of these MBs require good spatio-temporal resolution and suppression of the tissue signal. These requirements are met by using high-frame-rate plane or diverging wave imaging combined with tissue suppression methods. In this project, the effect of pulse inversion (PI) and harmonic filtering or singular value decomposition (SVD) filtering on the MB detection in slow flow was evaluated. This effect was measured in a soft-tissue-mimicking phantom containing a 400 μm diameter wall-less channel.
Methods: The US acquisition was done with a Verasonics V1 system, using a convex (C5-2) probe. Two sequences for coherent compound diverging-wave imaging were designed: the first for imaging in the fundamental (F) mode and the second for PI. The axial and lateral resolution were measured and the localization precision determined. Next, the effect of changing the number of compound angles, voltage, flow velocity, the receive mode (fundamental or harmonic), SVD-filtering and tissue motion on the MB detections was evaluated in four experiments.
Results: The results of the system characterization showed an average lateral & axial resolution in F-mode of 2.5 mm and 1 mm, respectively. In PI-mode the lateral & axial resolution was higher because of imaging at higher frequencies (2.0 mm and 0.8 mm, respectively). The MB localization precision was 20 μm lateral and 6 μm axial, from which we deduce that ultrasound localization microscopy improves spatial resolution with an average factor of 75. The results of the MB detection experiments showed a decrease of MB detections when the number of compounding angles increased. Possibly because of less false detections, since compound imaging results in improvement of contrast and a reduction in speckle and artifacts. No direct relation between the increase of transmit voltage and MB detection was found. In the SVD-filtered PI-mode data, the increase of flow velocity from 1 till 2 till 4 mm/s was accompanied by an increase in MB detections and a decrease in the false positive detections. At low flow velocities, the difference in spatial coherence between tissue and MBs was low which could have resulted in poor differentiation. Receiving in the harmonic-mode, resulted in a small spatial shift of the location of the MB detections because of asymmetry of the used radio-frequency filter. Besides, in the harmonic receive-mode the total number of MB detections dropped. A probable explanation is that less false MB detection were made because of suppression of flash artifacts. When tissue motion was induced, this led to higher MB detections in the non-filtered PI mode than in the stationary case. However, these can also be motion artifacts which are falsely detected as MBs. SVD-filtering or harmonic-filtering of these acquisitions resulted in practically zero MB detections.
Conclusion: We conclude that non-filtered PI results in more true-positive MB detections than harmonic-filtering and SVD-filtering when flow velocities are low. When tissue motion is negligible, PI-imaging results in good SR images, with a possible disturbance of flash artefacts.

Preface

This master thesis is written to complete the Msc Biomedical Engineering - Medical Physics at the TU Delft. My project work is done at the Utrecht Medisch Centrum, The Netherlands, at the Imaging department.

To start, I would like to thank everyone who was involved in this project for their support. Doing this project gave me the opportunity to work with a lot of people, from which I would like to thank a few in particular.

First I would like to thank my daily supervisor, Roel Deckers, for all the input you gave. Your creative ideas and encouraging words helped me to overcome the challenges faced during the project. Your enthusiasm for both the literature study and this project was priceless to me.

Secondly, I would like to thank my TU delft supervisor Rik Vos for your support and suggestions on how to proceed in this project. Especially during the writing process, your voice in the back of my head helped me to stick to my plan.

Finally I would also like to thank friends, family and fellow students. A special thanks goes to Hadi Mirgolbabaee for helping me with writing the scripts for the Verasonics. Our meetings were very helpful to me. To all my fellow researchers at the high-intensity-frequency-ultrasound group, thank you for the time at the UMC, for sharing your experiences in research and providing me with the advice I needed.

M.A. ter Wee
Utrecht, February 2021

Contents

1 Introduction

The ability to map microvasculature is of major importance in the clinical assessment of a variety of disease processes. For example, measurements of perfusion, size, vessel density and flow patterns can be translated to diagnostic markers for cancer [19]. These parameters are difficult to assess because of the limited resolution that is obtainable by diagnostic modalities.

In the past years, many research is done in the field of microvasculature imaging using standard diagnostic modalities. Magnetic resonance imaging (MRI), Computed Tomography (CT) and Positron emission tomography (PET) can reach a resolution in the range of 100 μm, 200 μm and several millimeters, respectively [7]. However, these resolutions are not high enough to map micro-vessels, which can have a diameter of 10μm. Optical techniques can generate an image on a 5μm scale, but are limited to a penetration depth of 1-3 mm. Micro-CT is able to reach resolution on a nano-meter scale, but this is not applicable in human imaging.

Ultrasound (US) imaging provides a cheap, non-ionising, real-time imaging tool. However, the maximal obtainable resolution is limited by the resolution-imaging depth trade-off. The resolution of the US image is determined by the wavelength of the transmitted wave (wavelength=speed of sound/frequency). The frequency in clinical scanners ranges between 1- 15 MHz, which results in a maximal obtainable resolution in the range of 100 μm. However, the high frequency signals are stronger attenuated by the medium which limits the US penetration at high frequency to several cm in soft tissue.

Super-resolution (SR) ultrasound breaks the compromise between resolution and penetration depth and is able to reach microscopic resolution at clinically relevant tissue depths. The microscopic resolution even goes beyond the fundamental diffraction-limit of wavelength/2 [3]. An approach into SR imaging is Ultrasound localization microscopy (ULM). This method relies on the dynamic appearance of microbubbles (MBs) in a flow circuit. As a result of the acoustic field, the MBs appear as point scatterers on the US image [36]. The scatterers can be traced back to their exact location by using the point-spread function of the US system [8]. The accumulation of multiple bubble locations results in the super-resolved image, that can reach a deeper detection limit than the regular high-resolution US image.

An important step in ULM is the detection of the MBs. The more MBs detected, the more evidence available to build the super-resolution image. To enable MB detection, the US acquisition must meet some requirements. The first is that the US acquisition should result in a sufficient number of frames so that MBs can be detected at multiple positions in the vessel. To avoid long acquisition times and to be able to trace individual MBs through the vasculature, the frame rate should be high. Tracing the MBs along the vasculature has also been reported as a criterion in the detection step: the MB detections are linked together in consecutive frames in order to distinguish MBs from noise [18]. The requirement can be met by using ultrafast ultrasound imaging.

The second requirement is that the US acquisition provides high-contrast images which make differentiation between the MB and the surrounding tissue possible. Let's take a look at the mechanisms that the MBs in the blood flow induce and in which way that can be used to differentiate them from tissue. The introduction of microbubbles (MBs) into the blood flow and insonification with an US wave triggers two responses. The gas inside the MB has a different compressibility than blood, forcing it into

volumetric pulsation at a high-amplitude in response to the acoustic field: at the positive half cycle of the US wave the bubble size decreases and in the negative half cycle the bubble size expands [20]. This pulsing is the strongest at a specific frequency: the resonance frequency. This resonance generates a secondary source of sound in the medium with at relative strong echo strength in comparison to the reflective tissue. However, especially in microvasculature where the MB concentration is low, the resulting fundamental image has poor contrast between the MBs and the tissue which limits their detectability. Their detection then relies on the dynamic appearance since MBs are carried along with the blood flow. Filters can be designed to distinguish the faster moving signals (MBs) from the slower moving signals (tissue). Such tissue suppression filters will be in trouble when the movement of the MBs between the frames is in the same extent as the tissue motion. This could be the case in the application of microvasculature US imaging, where the flow velocities are typically low.

In this case, we can look at an additional characteristic of the MB response to the acoustic field. For higher amplitudes, the pulsation of the MBs can become non-linear to applied acoustic pressure: the time in that the MB is compressed is relatively longer than the time that the MB is expanded. This is a result of the MB geometry and stabilising coating around the MB. These non-linearities give rise to second- and higher-harmonics in the US signal. The acoustic energy carried by these higher-harmonic frequencies is lower than the fundamental frequency. However, since the tissue generally generates less non-linear disturbance of the signal, the MBs and tissue signal components can be separated in the frequency domain.

Tissue suppression methods based on the dynamic characteristic and on the harmonic characteristic of the MBs are explored in this project. The first is pulse inversion (PI) in which a contrast image is built by transmitting two identical inverted pulses. When the returning echoes of these pulses are summed, the linear (tissue) signal components become zero and the nonlinear (MB) signal components are preserved [11].

The second method tested is harmonic-filtering of the received US signals. The higher harmonics that originate from the non-linear vibrations of the bubbles can be discriminated from the fundamental frequencies by applying a high pass filter in fast-time [25].

The third tissue suppression method tested in this project is clutter filtering. The state-of-the art approach to clutter filtering is Singular value decomposition (SVD) which uses the spatio-temporal differences between tissue and MB signals [15]. It is assumed that the tissue is highly time and space coherent in comparison to the flowing MBs. These differences in characteristics can be used to decompose the US signal in tissue and MB components. Rather than relying on the nonlinear frequency response of the MB, SVD is build on the incoherent spatial change due to their displacement [45].

Previous research studied the effect of spatio-temporal filtering and contrast imaging on the contrast-to-tissue ratio (CTR). Desailly et al. [15] showed that the CTR of SVD-filtered fundamental US images is similar to power-modulated pulse inversion (PMPI) and Doppler PMPI images if the flow is low (<5 mm/s) in a 5 mm diameter vessel. Voorneveld et al.[44] showed that SVD provides higher CTR than amplitude modulation (AM) + SVD, AM+Doppler filtering or AM alone at a flow velocity of < 100 mm/s in a large diameter vessel. Linear SVD in a non-flowing microvessel (300 μm) filled with MBs was compared to PI in a study by Zhu et al. [47]. They qualitatively compared the two methods and concluded that using SVD, the tissue-mimicking control tube was removed from the image while maintaining the contrast from the MBs. This was not achieved in the PI image: the tissue-mimicking tube was not removed from the image but the contrast of the MBs was preserved.

The question whether coherent compounding combined with pulse inversion and harmonic filtering or with SVD filtering results in good image quality for further SR processing remains unanswered. Furthermore, the application of these tissue suppression methods in measuring slow flow in a micro-vessel has not yet been investigated. This leads to the research question:

What is the effect of pulse inversion combined with harmonic- or with SVD-filtering on the number of MBs detections in ULM in a micro-vessel?

It is hypothesized that the number of MBs detected per series of imaging frames increases with the number of coherent compounding angles used. Coherent compounding increases contrast which allows for better MB detection [27].

The implementation of a pulse-inversion pulsing sequence is expected to enhance MB detection in comparison to a fundamental (F) pulsing sequence. In PI, the fundamental frequencies are cancelled which leads to higher contrast between MBs and tissue [9].

Harmonic filtering of the received signal will have a different effect on the signals transmitted in a PI transmission-scheme than in the F transmission-scheme. In the PI-scheme, the fast-time high pass filtering results in suppression of the flash artifacts [29], which is expected to improve MB detection. In the F-scheme, the frequency band of the center-frequency is expected to partly overlap with the frequency band of the second harmonic [35]. The signal at the center-frequency is generally higher in amplitude and is therefore expected to overrule the signal component corresponding to the non-linear vibrating MBs.

The fourth hypothesis is that the application of SVD filtering in the F- and PI-mode results in a higher contrast between the MBs and the background, which enables good differentiation between the MB and tissue signal components. Even though the displacement of the MBs between the consecutive frames is low, using both the spatial and temporal coherence to differentiate the MBs from the tissue will improve the operation [13].

Finally, the number of MBs detected in the non-filtered PI-mode images is expected to be low if large tissue motion is induced. Strong tissue motion induces phase decorrelation between the two pulses which results in a leakage of fundamental frequencies in the PI-signal, resulting in flash artifacts [37]. It is hypothesized that filtering with a fast-time high pass filter suppresses these flash artifacts and results in good contrast sensitivity, as previously described by Philips et al. [29]. Finally, it is expected that SVD will not be able to distinguish the moving tissue from the MBs since spatial coherence between these signal components is high and they cannot longer be separated by SVD [13].

This report presents *in vitro* measurements of bubble detection under variation of pulsing sequences and filtering of high frame rate diverging wave imaging. A simple MB detection algorithm based on the method described by Viessman et al. (2013) is used to quantify the number of MBs detected [43]. The results are divided into two parts. The first part includes the results of the characterization of the system, by measuring the point-spread-function (needed as input for the MB detection algorithm) and the localization precision of the system. The second part presents the results of the MB flow experiments in sets of parameter variations.

2

Background

To provide the reader with background knowledge that is assumed to be present in the subsequent chapters, this chapter presents the background of the the techniques used in this research.

In the past 30 years, super-resolution (SR) has been a topic among different research groups. It is a collective name for separating two objects that lie within the classic resolution limit of the imaging system [42]. SR became of interest for the US community after new developments in the world of optical microscopy [3]. Fluorescence-stained molecules were localized sub-wavelength and reconstructed into super-resolution images: photoactivated localization microscopy (PALM) and stochastic optical reconstruction microscopy (STORM). This allowed to map the location of the point scatterers within the diffraction limit, using visible light. Shortly after it was Couture and colleagues who first managed to build a super-resolution ultrasound image [10]. Instead of light, they used ultrasound waves and instead of fluorescence staining they used ultrasound contrast agent: microbubbles. The localization of these bubbles within the diffraction limit and accumulation of multiple bubble positions is referred to as Ultrasound localization microscopy (ULM). The individual bubble locations can be tracked between adjacent frames to derive flow direction and build velocity maps *in vivo* [5]. This is also reported as a method to differentiate MBs from noise by linking the detections between consecutive frames [18].

The steps taken in the SR-imaging pipeline are shown in Figure 2.1. The first step (A) refers to the US acquisition of the MB flow. The MBs should be imaged at a sufficient number of positions to facilitate the following steps. This requires good spatio-temporal resolution and a sufficient number of imaging frames. The second step (B) is the detection of the MBs, which includes the differentiation

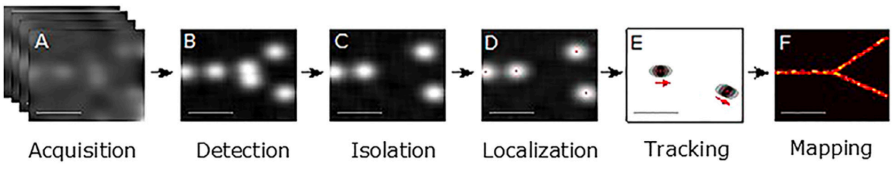

Figure 2.1: Pipeline describing the steps in Ultrasound localization microscopy (step A - D,F) and velocity mapping (step E - F). (A) The ultrasound acquisition of a MB flow setup. (B) The detection of the MBs on the series of frames. (C) The isolation of the separate MBs, rejection of the overlapping MB signals. (D) The localization of the isolated MBs. (E) The tracking of the MB positions in consecutive frames. (F) The mapping of either the accumulated MB locations or the velocity vectors. *Image from Christensen-Jeffries (2020) [6]*

of the MBs from the background. Depending on flow velocity, acquisition power and the transmitted frequency, the MBs can be discriminated from tissue based on their motion, disruption and non-linear resonance [4].

The third step (C), isolation, refers to the spatial separation of the detected MBs. If two MBs overlap in the image frame, this compromises the localization step and these bubbles are erased from the frame. Advanced separation steps or a more obvious method, lowering the MB concentration, can be applied to avoid incorrect localization [6].

The fourth step (D) is the localization of the isolated MBs. The microbubbles appear as point scatterers and in order to form a super-localized image, these scatterers are traced back to a single MB location [3]. On the RF-data, the back-scattering MB appears as a parabola which can be fitted to the time-of-flight to the transducer elements to find its originating position [8]. A second approach is finding the MB location in the beamformed data in which the MB appears as a high intensity blob. Its location can be identified by calculating the intensity-weighted center of mass or Gaussian fitting [5, 43].

Accumulation of the superimposed MB positions can form a high-resolution Maximum Intensity Projection, a convenient tool to map the microvascular structure. Quantitative velocity maps can be withdrawn from the MB locations by drawing velocity vectors between consecutive bubble positions [18]. This sums up the final two steps (E&F) of the SR pipeline in Figure 2.1.

2.1. Acquisition

The challenge of ULM in microvascular flow is that, to achieve accurate mapping, a sufficient number of MB must be detected in the blood flow [18]. To prevent MB signals to overlap, the concentration of MBs in the *in vitro* setup is limited [6]. In the clinical situation, MB concentrations in the microvasculature are low because the chance of an MB moving into a microvessel is dependent of its size [32]. The smaller the size, the lower the number of MBs passing through that particular branch. Collecting a sufficient number of MB detections thus requires a large number of frames.

In order to keep the acquisition time low and have sufficient temporal correlation, high frame rate imaging is called for. This can be accomplished by using plane or diverging wave imaging instead of conventional line-by-line imaging. A second advantage of using plane or diverging wave over line-by-line imaging is the reduction in acoustic pressure [9]. In ultrafast ultrasound, a number of plane wave transmissions at lower amplitudes can be compounded to result in similar image quality as in line-by-line at higher amplitudes [27]. In that way, the disruption ratio of the MBs can be minimized.

2.1.1. Transducers

The modern ultrasound transducer consists of an array of piezoelectric elements which convert electric into acoustic energy and vice versa [21]. Sending waves into the medium and receiving their echoes (phase and amplitude) and transform these into an electric signal. The waves sent into the medium are reflected or scattered back to the transducer, or are completely absorbed by the medium. The heterogeneous medium reflects pressure waves because of differences in acoustic impedance, the product of density and particle velocity [21]. The envelope of the received echo constructs the grey-scale image.

The wave transmitted into the medium can be split into a three dimensional coordinate system relative to the transducer. The three planes are shown in Figure 2.2. The lateral direction is parallel to the transducer elements along the long axis, the axial direction perpendicular to the array travelling into the medium and elevational parallel along the short axis of the array.

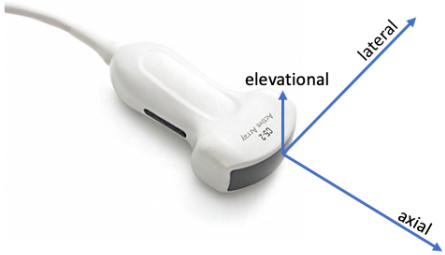

Figure 2.2: Convex (C5-2) transducer with scanning directions. For the 2D image: the lateral direction represents the horizontal axis, perpendicular to the direction of the beam, the axial direction the vertical axis parallel to the beam and the elevational directions translates to the thickness of of the slice.

The alignment of the piezoelectric elements and transmit delays determine the area in which the waves are sent, the scanning format. The transmit delays of the convex probe as shown in Figure 2.2 can

be designed to transmit a focused, plane or diverging wave. For this project we used a curved linear transducer (C5-2) with 128 elements in which all piezoelectric elements transmitted an unfocused wave simultaneously, resulting in a divering wave. The scanning format that corresponds to this design is shown in Figure 2.3.

The imaging depth (ED in Figure 2.3) along the axial axis cannot be infinitely long, since this parameter is limited by two factors. The first is the absorption of acoustic energy of the propagating wave by the medium: attenuation [21]. The degree of attenuation is dependent of the frequency: higher frequency signals are more attenuated by the medium [2]. The second factor is related to the physical imaging depth when imaging at a high frame rate. The travelling time of the wave into the medium and back to the transducer along the longest path must be shorter than the pulse repetition time. This relation is given by,

$$ED + s_{max} = c * t_{min} \tag{2.1}$$

in which c is the speed of sound in m/s, t_{min} the pulse repetition time and s_{max} the longest path which runs from the lower corner to the opposite-sided element. The longest path in the convex probe

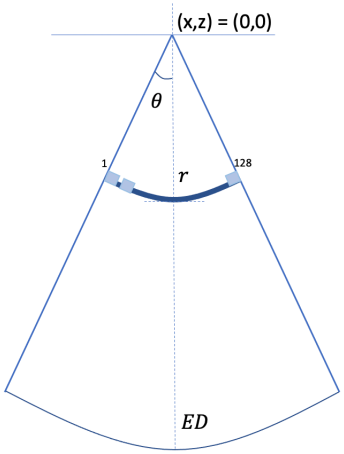

Figure 2.3: The scanning format of a curved linear array with 128 elements, when imaging with a diverging wave. θ is the angle of curvature of the array, r the radius or the distance from the origin to all elements on the array and ED the normal distance from he element to the maximal depth of the scanning format.

scanning format in Figure 2.3, is described by the radius of the scanner (r), the scanning angle θ and the end depth (ED):

$$s_{max} = \sqrt{(ED + r)^2 + r^2 - 2r(ED + r)\cos 2\theta}. \tag{2.2}$$

For example, when imaging at a pulse repetition time of 200 μs in a medium with a speed of sound of 1540 m/s, the maximal end depth is 11 cm.

2.1.2. Plane/diverging wave imaging

Plane wave or diverging wave transmissions enable ultrasound imaging at ultrafast frame rates [39]. The concept is based on parallel processing of an entire image frame from one acoustic pulse [27]. The resulting frame rate is equal to the pulse repetition rate, which depends on the maximum imaging depth.

Delannoy et al. (1979) were the first to propose parallel processing, although computational power was still limited at that time [12]. It was Fink and colleagues (1999) who first achieved plane wave imaging at frame rates of 5kHZ for the application of real-time shear propagation imaging [31]. Many research groups around the world ever since explored the optimization of these plane wave emissions. Lu et al. proposed the transmission with a plane wave, while receiving in limited diffraction beams of different parameters. Hu et al. (2010) proposed the use of retrospective filtering to enhance the spatial resolution and contrast [23]. All this pioneering work contributed to the method that is nowadays often used for ultrafast ultrasound acquisition: Coherent plane wave compounding.

2.1.3. Coherent compounding

The lack of transmit focusing in the plane or diverging wave emissions results in poor image quality in terms of signal-to-noise ratio and spatial resolution [39]. By coherent combination of multiple steered wave transmissions, the image quality can be restored [27]. Coherent compounding leads to reduction in side lobe levels, improving both spatial resolution and signal-to-noise ratio. Furthermore, Montaldo et al. [27] found that by using plane waves, less wave transmissions at different angles are needed to obtain the same image quality as in line-by-line imaging.

2.1.4. Image formation/Beamforming

After each individual plane/diverging wave transmission, the received signal (RF) is delayed to derive each location (x, z) in the image. The final image (s) is formed by coherent summation of the time delayed RF-data:

$$s(x,z) = \int_{x-a}^{x+a} RF(x_1, \tau(x_1, x, z))dx_1. \tag{2.3}$$

The time delays are determined by the path travelled from the transducer (x_1) to the focal point in the image and back (Figure 2.4).

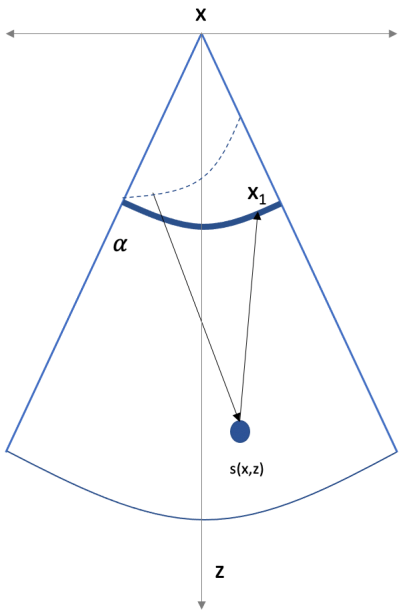

Figure 2.4: Schematic overview of a the path travelled by a single wave after angular steering. The starting point of the wave is placed after the transducer array by applying transmission delays.

In plane/diverging wave compounding, this path is characterized by the angle (α) in which the beam is transmitted:

$$\tau(\alpha, x_1, x, z) = \tau_{go} + \tau_{back} = \frac{z\cos\alpha + x\sin\alpha + \sqrt{z^2 + (x - x_1)^2}}{c}. \tag{2.4}$$

Coherent recombination of the beamformed data from different angles results in the final compounded image. The summation of the beamformed data is performed prior to taking the envelope, so the phase information is still intact. After coherent summation, the envelope of the beamformed signal result in the US image.

2.2. Spatial resolution

The spatial resolution of the grey-scale image is determined by the wavelength of the transmitted wave, which is related to the frequency (f) and the speed of sound in the medium (c),

$$\lambda = \frac{c}{f} \tag{2.5}$$

which is approximately 1540 m/s in soft tissue in human [21]. The inverse relation between wavelength and frequency implies that a finer resolution can be obtained at higher frequencies. However, two remarks to this have to be made.

The first is that high frequency signals are stronger attenuated by the medium. Thus, an increase in frequency comes at the cost of the imaging depth. The second remark is that resolution is diffraction-limited because of the finite size of the elements. In practice, this means that two objects lying closer than a half-wavelength of the transmitted beam together, cannot be resolved [28]. To achieve US imaging at fine resolution at sufficient imaging depths, super-resolution ultrasound makes its introduction.

2.3. Tissue suppression

In order to improve the MB detection during microvasculature flow imaging, the US imaging requires tissue suppression. The aim of these filtering methods is to separate the MB components from the tissue and noise components. In general, the tissue filtering can be executed in two time domains: slow-time and fast-time filtering.

In slow-time filtering, the change of the signal between consecutive frames is used to differentiate the rigid tissue from the moving scatters. Therefore, it is assumed that the flow and the tissue components can be separated based on difference in spatial en temporal characteristics [13]. MBs are carried along with the blood flow and produce a strong echo that moves in-between consecutive frames. This results in a Doppler frequency shift (temporal characteristic) and a decrease in spatial coherence in comparison to the tissue signal components (spatial characteristic).

In fast-time filtering, the higher-harmonic frequency signals are filtered from the received signal in each frame. The frequency band of the transmitted and the received signal differ because MBs introduce higher harmonic frequencies, most notable at twice the transmitted frequency [20]. However, the fundamental component partly overlaps with the second harmonic band (Figure 2.5).

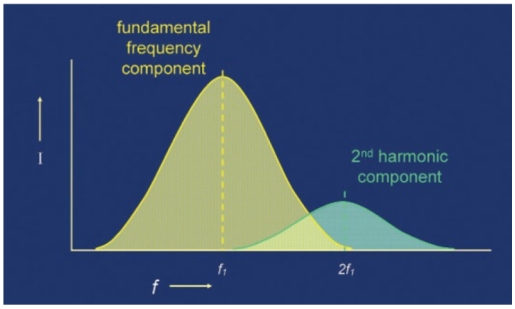

Figure 2.5: Graphic overview of the fundamental (f_1) and second harmonic ($2f_1$) frequency bands. The spectra of the fundamental frequency component (tissue) and the second harmonic component (MBs) overlap and the fundamental signal component typically has a higher intensity, fading out the second harmonic echoes. *Image from Starkoff 2014 [35]*

Ideally, the two bands are narrowed and the second harmonic is amplified for easier discrimination. However, this problem knows two trade-offs [33]. The first is the contrast/resolution trade-off which states that to diminish the overlap, the bandwidth of the transmitted pulse should be narrowed. This implies lengthening of the pulse length, which comes at the cost of the axial resolution. The second trade-off concerns the power-dependency of the second harmonic. The intensity of the returning echo is enhanced by increasing transmission power. However, this increase in transmission power induces MB disruption.

Advanced filtering methods in both the slow-time and the fast-time domain can be applied to increase the contrast between the MBs and the tissue and improve MB detection. The methods explored in this project are described below.

2.3.1. Contrast-enhanced ultrasound imaging

In ultrasound using contrast-specific detection schemes, images are formed by applying multiple transmit pulses. The pulsing scheme is realized by transmitting multiple pulses of varying amplitude or phase [38]. Examples are pulse inversion (PI), amplitude modulation (AM) and a combination of these two: power modulated pulse inversion (PMPI). For this project we use pulse inversion, in which the pulsing scheme consists of two identical yet sign-reverted pulses which are transmitted at a high pulse repetition period. The echo of the linear responding objects of the second pulse in the sequence is a sign-reverted copy of the echo of the first pulse, and the sum of these received echoes is zero [11]. In the presence of a MB, the two pulses in the sequence do not sum to zero. In that case, the summed signal can undergo standard beamforming to form a non-linear grey-scale image.

From a slow-time filtering point-of-view, the displacement of the MBs between the pulse transmissions cause a phase shift between the returning signals. This shift is not cancelled out and the PI-signal contains energy corresponding to the moving MBs.

From the fast-time filtering point-of-view, the summation of the two sign-reverted pulses is nonzero because the MBs partly resonate at higher-harmonic frequencies, most notable at twice the center-frequency [20].

Contrast imaging cancels out both the contrast-resolution and the power-dependent trade-offs. The pulse sequences make use of the entire bandwidth of the received signal, which means no trade-off between bandwidth and axial resolution. Furthermore, contrast imaging uses multiple low transmit power pulses, so MB disruption can be minimized [9].

A first disadvantage of contrast imaging relates to the frame rate. Pulse-inversion requires a multiple-transmit pulse sequence which reduces the frame rate by a factor two. A second disadvantages is that the PI-signal can be disturbed by higher-harmonics that originate from non-linear acoustic wave propagation through the tissue. However, at low mechanical indices, this contribution has proven to be insignificant [38].

2.3.2. Harmonic receive mode

The second approach to differentiate the signal components is harmonic filtering: high pass band filtering in the fast-time domain. This can also be seen as restricting the receive mode to only high frequency signals, hence the name used in this work: Harmonic receive mode. This operation filters in the Fourier domain using a cut-off frequency value [24]. All frequencies below the cut-off value are attenuated and above the value can pass freely. By choosing the cutoff-value in-between the peaks shown in Figure 2.5, the fundamental frequency band is filtered out and most of the remaining acoustic energy is located in the second-harmonic frequency band. The frequency band is still partly overlapped by the fundamental band and therefore the MB signal might be overruled by the tissue signal. The intensity of the MB signal components must be sufficient for it not to drown under the tissue signal component. Thus high pass filtering does not completely cancel out the power-dependency trade-off.

Fast-time high pass filtering of the pulse-inverted signal can contribute to the suppression of flash artifacts. The displacement of tissue can, just like the MBs, induce a phase-shift which is not summed to zero in a pulse-inversion sequence. This causes leakage of fundamental frequencies in the PI-signal which appear as rapidly changing bright spots on the PI image. These spots can be mistaken for MBs. High-pass filtering of the PI-signal cancels these fundamental frequency leakages, which results in a signal at the second-harmonic frequency [29].

2.3.3. Singular value decomposition

A third method of tissue suppression assumes that the signal components originating from noise, tissue and microbubble flow can be differentiated based on the spatio-temporal coherence energy [13].

In comparison to the MB flow signal, tissue gives a higher intensity signal and is more spatio-temporal coherent. Thus when the US signal containing the three components is decomposed using singular value decomposition, the tissue components built up at the lower rank (See figure 2.6)

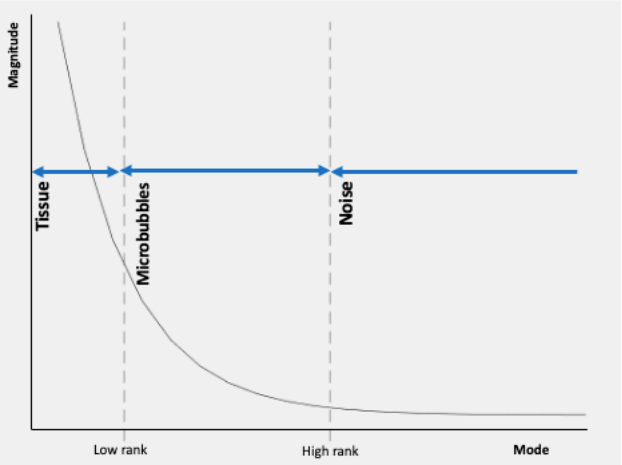

Figure 2.6: Illustration of the accumulation of the tissue, MB flow and noise signal components in the received signal. The vertical axis show the arbitrary value Magnitude which describes the signal intensity and coherence energy. The tissue signal is typically located in the low rank mode, where spatial coherence energy and signal intensity is high. The noise is low coherent and has low amplitude. The MB signal component lies in between.

Prior to the decomposition, the data is organized in a Casorati matrix. This is a 2D matrix in which each column represents the vectorized image frame at a moment in time. By using ultrafast ultrasound, a large sequence of simultaneous US is available to arrange vertically in the matrix.

Singular value decomposition subdivides the Casorati matrix into temporal and spatial vectors, which are linked by the diagonal matrix. The nonzero values of the diagonal matrix correspond to the rank (or mode in Figure 2.6) Filtering out of the higher spatial coherent signal (tissue) is achieved by removing the low rank singular vectors from the raw US signal.

3

Methods

3.1. Ultrasound equipment & acquisition settings

The ultrasound acquisition was done with the Verasonics V1, a four board system with 256 transmit and 128 receive channels connected to two scan-head connectors (Verasonics, Kirkland Washington, USA). Scan-head 1 was connected to the C5-2 transducer which has 128 elements in a convex array. The system provides a tool for transmitting, receiving and processing of ultrasound. These sequences are designed on a Matlab-based interface and consist of a collection of objects bundled in structures. These structures are loaded into a .mat-file and executed by Verasonics Script eXecution (VSX) to start image acquisition.

The first sequence designed for this project generated a multiple transmit acquisition with transmit delays to generate a coherent angular compounded image. We call this 'Fundamental (F) mode'. The second sequence was designed to enable contrast-imaging and uses a pulse inverted approach. This indicates that each uneven numbered pulse in the pulse train has an initial positive polarity and each even pulse in the pulse train an initial negative polarity. We call this 'Pulse inversion (PI) mode'.

The frame rate of the acquisition depends on the pulse repetition period (PRP), the imaging-mode (i) and the number of compound angles (na) in the following relation:

$$FR(Hz) = \frac{1}{PRP(s)\ na\ i} \tag{3.1}$$

in which $i = 1$ in Fundamental mode and $i = 2$ in Pulse inversion mode. The PRP was set to 400 μs.

The pulse rates were too high to process and reconstruct in real-time, so the radio-frequency (RF) data was stored into the receive buffer and reconstructed afterwards. The RF data was organized in 25 'superframes', each containing the RF-data of 200 transmission events. This gave a maximum of 1000 images for 5 compound angles, 500 images for 10 compound angles and 250 images for 20 angles. For F-mode the recording time was 2sec and for PI-mode 4 sec.

The transmit frequency was 3.2 MHz. The bandwidth was set to the default, which is 60% of the center frequency. The RF-data was sampled (by the analog/digital (A/D) converter) at 4 times the center frequency. The receive-buffer, containing the high frame rate RF-data, was stored and reconstructed into grey-scale images on the Verasonics.

3.2. Characterization of the imaging system

The point-spread-function (PSF) characterizes the response of the imaging system to an object smaller than the diffraction limit. The spatial resolution is defined by the axial and lateral full-width-half-maximum (FWHM) of the PSF [40].

The FWHM of the PSF was measured in a container (8x8x9 cm^3) filled with degassed-water and an ultrasound absorber at the bottom. At a height of 3 cm, a 200 μm cupper wire was placed in the water-filled container. This wire was estimated to be smaller than the diffraction limited resolution of the scanner and mimicked a point scatterer. The transducer was aligned perpendicular, so that the

cross-section of the wire could be measured. This same setup was used to measure the localization precision.

3.2.1. Measurement of axial & lateral resolution

The measurement of the axial & lateral resolution was repeated at different acquisition settings: number of compound angles, angle between angular transmissions (dθ), transmission mode, distance from transducer to wire and voltage. An overview of these settings is shown in Table A.1 in Appendix A.1. In each acquisition setting, 20 frames were recorded and the raw intensity data for each frame was stored. The background noise of the system was estimated by the mean intensity value and was used as an intensity threshold for all the frames in the dataset.

The measured FWHM ($FWHM_{measured}$) is a convolution of the size of the finite wire ($FWHM_{wire}$) and the FWHM of the PSF ($FWHM_{PSF}$) [7]. Deconvolution results in the values of the $FWHM_{PSF}$,

$$FWHM_{PSF} = \sqrt{FWHM_{measured}^2 - FWHM_{wire}^2}. \tag{3.2}$$

To measure the axial and lateral FWHM from the data, a 2D Gaussian PSF model was fitted to the intensity data using a non-linear least square algorithm. The Gaussian model is given by

$$f(x,y) = a_i e^{-\frac{(x-\mu_x)^2}{2\sigma_x^2} + -\frac{(y-\mu_y)^2}{2\sigma_y^2}}. \tag{3.3}$$

in which a_i is the amplitude, μ_x and μ_y the location of the center of the Gaussian function, σ_x and σ_y are the standard deviations of x and y. The lateral FWHM was then found by solving $f(x,\mu y) = \frac{1}{2}a_i$ and the axial FWHM by solving $f(\mu x, y) = \frac{1}{2}a_i$.
The average of the lateral FWHM of the PSF over the 20 frames was substitute for the lateral resolution of the US system. The average axial FWHM was substitute for the axial resolution. The standard deviation of the estimated FWHM in all 20 frames was the measurement error.

3.2.2. Localization precision

Four methods to determine the location of the wire reflection were tested. The location of the wire reflection was determined in 20 frames and the standard deviation was calculated to evaluate the localization precision of each method. The first method was based on the standard MATLAB-function, *RegionProps* which determines the center of a connected components region [26]. The second method was to calculate the intensity-weighted center of mass (COM) of the point scatterer using the following equation

$$[Cx, Cy] = \frac{\sum_i I(x_i, y_i)[x_i, y_i]}{\sum_i (x_i, y_i)} \tag{3.4}$$

where i is the pixel integer, $I(x_i, y_i)$ the intensity of the pixel located in (x_i, y_i) and $[x_i, y_i]$ the coordinates. For this method it was assumed that the centroid of the 'blob' corresponds to the location of the scatterer. The third method was an optimization of the location that is found in method 2. To determine the horizontal coordinate of the scatterer, a Gaussian fit in the axial profile (at y equals the intensity-weighted COM found in method 2) was made. This Gaussian model fits peaks following,

$$y = \sum_{i=1}^{n} a_i e^{-(\frac{x-b_i}{c_i})^2}. \tag{3.5}$$

where a_i is the amplitude, b_i the location of the center of the Gaussian function and c_i the standard deviation of x. The same process was repeated to determine the location of the vertical coordinate of the wire reflection. Now, the Gaussian model was fitted at x equals the intensity-weighted COM found in method 2. The fourth method that was tested is least-square fitting of a 2D Gaussian model as described by Equation 3.3. The location of the wire reflection was obtained by calculating the position of the center of the Gaussian function (μ_x, μ_y).

The parameter settings used to determine the localization precision were 10 angles, $d\theta = 0.04$ rad, pulse inversion mode, depth 4 cm and 20V. These settings were most representative for the settings used in further experiments.

3.3. MB detection

The effect of changing the pulsing scheme, higher-harmonic imaging and filtering on MB detection was evaluated in an *in vitro* experiment in which microbubble flow in a micro-vessel was mimicked. The effect was quantified by using a simple MB detection algorithm which is elaborated in Section 3.3.3.

3.3.1. Setup

The microvessel embedded in tissue was mimicked by using an agar gel phantom. It consisted of a 8x8x12 cm^3 container which was poured with 2% agar gel. The microvessel was constructed by stretching a 400 μm nylon wire between the walls. The wire was removed after the gel solidified to form a wall-less channel. The in- and outlets of the channels were supported by needles, which allowed the MB solution to flow through the channel. An illustration of the setup is shown in Figure 3.1.

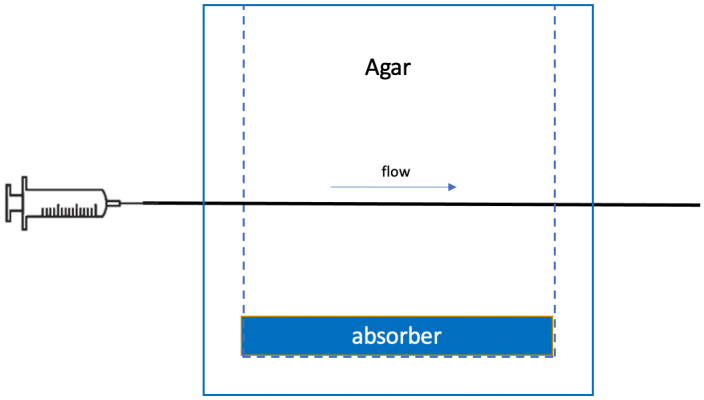

Figure 3.1: Illustration of the experimental setup used during the flow acquisition experiments. MBs flow was from left to right.

The MB solution was prepared following the instructions provided by the manufacturer. The SonoVue (Bracco, Milan) MBs were prepared by injecting 5 mL sodium chloride solution into the vial. This led to approximately 1-5$\cdot 10^8$ MBs per mL. This was diluted to a 1:28 solution, resulting in approximately $7 \cdot 10^6$ MBs per mL. The solution was administered into the channel using a 50 mL syringe with a small stirring magnet to keep the MBs in solution. The syringe was placed in a flow pump (Harvard apparatus pump 33) to produce a continuous flow.

3.3.2. Acquisition parameters

During the MB detection experiments, the pulsing scheme, filtering and other acquisition parameters were varied to measure their effect on the number of MB detections. The parameters tested are listed in Table 3.1.

Parameters	Settings
Transmission mode	F-mode, PI-mode
Receive mode	Fundamental, Harmonic
Number of angles	5, 10, 20
Flow	1, 2, 4 mm/s
Voltage	8.8, 11.3, 13.7 V
Slow-time filtering	None, SVD
Tissue motion	No, Motion

Table 3.1: The parameters varied in the MB detection experiments. The effect of changing the parameters on the frames is quantified as the number of MB detections.

To avoid confusion about the acquisition mode of the reconstructed images, a distinction between transmission mode and the receive mode was made. The transmission mode indicates whether the pulsing scheme (of a single compound angle) contains a single pulse like in fundamental-mode ultrasound (F-mode), or two sign-inverted pulses like in pulse-inversion mode (PI). Note that imaging in

F-mode resulted in a 2 sec acquisition at a frame rate of 500 Hz, 250 Hz or 125 Hz for 5,10 and 20 angles and PI-mode in a 4 sec acquisition at a frame rate of 250 Hz, 125 Hz or 63 Hz for 5,10 and 20 angles.

The receive mode indicates whether the complete received frequency band is used to reconstruct the image (Fundamental) or the high-pass filtered frequency band is used to reconstruct the harmonic image (Harmonic). The fast-time high pass filtering was performed using a Cheby II filter with a -6 dB drop-off at 1.5 times the center frequency (at 4.8 MHz).

The number of angles refers to the number of compounding angles used to form one image frame. Given that the Verasonics Receive buffer size was fixed to 5000 acquisitions, the increase of compound angles led to a smaller total number of frames in the dataset. Using 5 compounding angles resulted in 1000 frames, 10 compounding angles in 500 frames and 20 angles in 250 frames.

The flow during the acquisitions was continuous and varied to approximately 1 mm/s, 2 mm/s and 4 mm/s in the channel.

The transmission voltage was varied to 8.8, 11.3 and 13.7V. The voltages were kept as low as possible to minimize MB disruption.

The recorded signals were either not filtered in slow-time, or filtered with SVD. The SVD-filtering algorithm followed the publication by Demené et al. [13]. The raw RF data was divided in 5 subsets, resulting in an ensemble length of 1000. The cutoff rank was determined by applying the guideline given by Yu & Lovstakken [46]. This is based on the assumption that the eigenvalue spectrum flattens once blood and thermal noise signals are introduced. Therefore, the energy decrease between two consecutive eigenvalues ($n-1$ and n) is less than 1%, i.e. $\frac{\sigma_n}{\sigma_{n-1}} > 0.99$. No high-rank cutoff value was used.

To explore the effect of moving tissue during the acquisition, tissue motion was induced by simply kicking the table on which the setup was placed.

3.3.3. MB super-localization algorithm

The automatic detection of MBs in the recorded frames was done by a self-designed MATLAB algorithm based on the publication by Viessman et al. [43]. This method required several image processing steps which are discussed below. All steps were performed on the beamformed intensity data.

The first step is a total intensity threshold which was used to make a coarse separation between the frames that potentially contain MBs and the frames that do not contain MBs. This threshold was determined by the average intensity value in the region outside the MB channel. The no-MB frames were used to design a rolling-background filter. The structure element used for this operation was a non-flat (real-valued) ball object. The filter-ball 'rolled' over the no-MB frames flattening the background pixels, while preserving the channel edges. This filter was applied to the potential-MB frames to suppress background.

The filtered frames containing the potential MBs were thresholded to reject low intensity signals. The size of the connected components of the intensity signals above the threshold was compared to the size of the area covered by the PSF. Areas smaller than the PSF area were padded to zero. Areas that had a similar or larger size than the PSF were considered potential MBs.

In the next step, a 2D Gaussian least-square fit (Equation 3.3) was performed at the potential MB areas. The starting point of the fit was the center of the connected components of each of the areas. This resulted in a table in which the Gaussian parameters (μ_x, μ_y, σ_x, σ_y) and the Goodness of the fit (GOF) were stored of each fitted MB. The peak of the Gaussian fit was considered to represent the MB location. The GOF-parameter R^2 was used as a cutoff to differentiate MBs from the fitted noise.

The results of the MB detection experiment were quantified as the number of MBs detected along the lateral dimension and shown in histograms. Additionally, the detected MBs were shown in a super-localized US image, in which the MBs locations were displayed as a Gaussian blob, with a lateral and axial standard deviation of 20 μm and 6 μm, respectively (based on the result of the localization precision experiment). The brightness of the blob was determined by the R^2-value which described the goodness of the Gaussian fit for localization. Additionally, the locations of the detected bubbles were compared with the estimated location of the channel. Because the exact location of the channel was not known, this region was estimated by 4 times the channel diameter (800 μm each side). The number of MBs detected outside the channel was calculated as the false positive fraction (%) on the total

number of MBs detections.

The locations of the detected MBs in the frames without filtering, after SVD-filtering and after Harmonic-filtering were compared using scatter plots. The MB location found before and after filtering was considered similar if they lied within two times the Euclidean distance of the lateral & axial localization precision apart. This distance was $2\sqrt{20^2 + 6^2} = 42\mu m$.

4

Results

4.1. Characterization of the imaging system

This section shows the results of the Characterization of the imaging system, which contained two experiments. Both experiments used the same setup: a water-container in which a 200 μm diameter copper wire was placed. The reflection of this wire was used to characterize the PSF of the imaging system. In the first experiment, the resolution was determined by measuring the lateral & axial Full-width-half-maximum (FWHM) of the PSF of the system. This measurement was repeated for 20 frames and the results were plotted. The acquisition settings were varied to determine their effect on image resolution. The results of these variations are shown in Appendix A.1, section 4.1.1 shows a selection of these variations.

In the second experiment, the position of the copper wire was determined in each of the 20 frames. The standard deviation of the 20 locations defined the localization precision of the method used. Four methods to determine the location were compared. The results of this experiment are shown in section 4.1.2.

4.1.1. Measurement of lateral & axial resolution

The results of the resolution measurements using different compounding angles in F- and PI-mode are shown in Figure 4.1 and Figure 4.2, respectively. The black dots denote the median of the data-points, the whiskers the minimal and maximal values and the bars the first and third quartiles. The images were acquired in 'complete' receive mode, at 20V and the cupper wire placed at 4 cm depth.

The lateral resolution increased from approximately 3 mm to 2 mm between the compound angles na=5 and na=20 in F-mode (Figure 4.1). This improvement in lateral resolution was accompanied by a wider distribution of the data-points. In PI-mode, the increase of the number of angles showed no direct relation to the change in lateral resolution. The frames acquired with 10 or more compounding angles, resulted in a larger distribution of the data-points than in na=5.

The lateral resolution measured in PI-mode was smaller than F-mode for 5 and 20 angles. Angular compounding using 10 or 15 angles in PI-mode showed a similar resolution as F-mode using 15 or 20 images. The measurements in PI-mode measurements were less distributed than in F-mode. The average lateral resolution in F-mode was 2.5 mm and in PI-mode 2 mm.

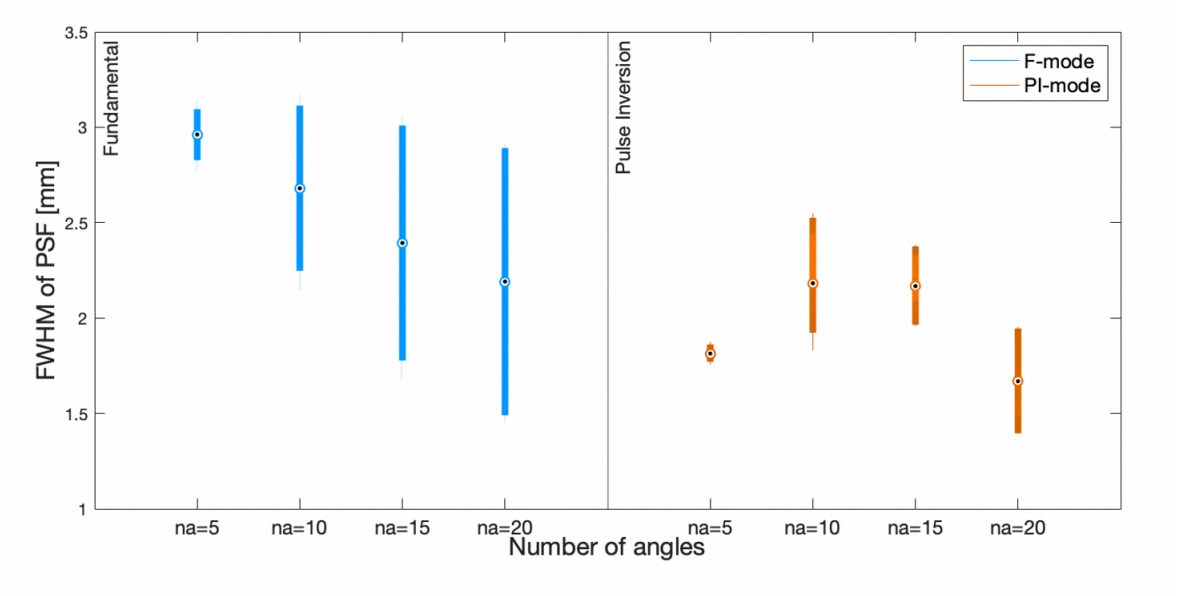

Figure 4.1: The lateral resolution measured by the horizontal FWHM of the wire reflection. Acquisition was performed in complete receive mode, at 20V and with the copper wire placed at a imaging depth of 4 cm. The F-mode showed an increase in lateral resolution when number of steering angles increased. In PI-mode, no direct relation was derived. In both modes, the increase of the number of angles resulted in a larger distribution of the data-points.

In F-mode, the axial resolution showed a small (~0.1 mm) decrease between 5 and 20 compound angles (Figure 4.2). The distribution of the measurements did not differ between the number of compounding angles. In PI-mode, the effect of coherent compounding on the axial resolution was smaller than 0.2 mm. The resolution found in the 5 and 20 angle compound images was similar. The na=10 resulted in the lowest axial resolution and the largest distribution.

In general, the axial resolution in PI-mode was slightly higher than in F-mode for all compound angles. This difference was approximately 0.2 mm. The average axial resolution in F-mode was 1 mm and 0.8 mm in PI-mode.

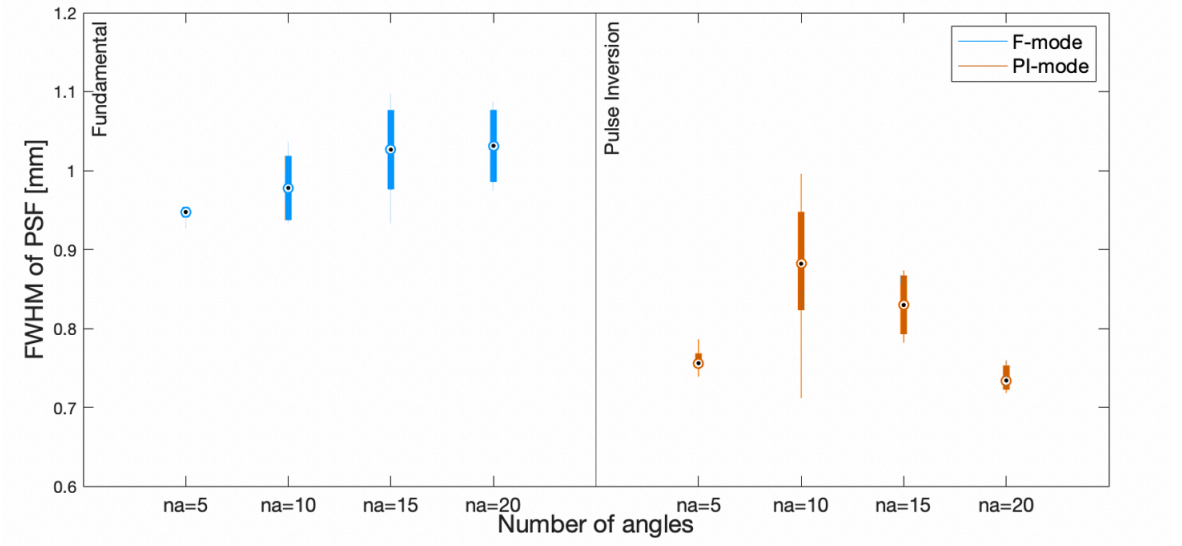

Figure 4.2: The axial resolution measured by the vertical FWHM of the wire reflection. Acquisition was performed at 20V at an imaging depth of 4 cm. In F-mode, the increase of number of angles was accompanied with a small (~0.1 mm) decrease in axial resolution and an increase in distribution of the data-points. In PI-mode, no obvious relation between the number of angles and the FWHM was drawn from the data. The na=10 and na=15 resolution showed the largest distribution.

The axial resolution was for both the F-mode and the PI-mode approximately a factor 3 lower than the lateral resolution. The distribution of the data-points was also smaller in the axial dimension than in the lateral dimension.

In the F-mode, the relation between the compounding angles and the lateral & axial resolution was inverse: the increase of number of compound angles resulted in an increase of lateral resolution and a small decrease of axial resolution. In PI-mode, the trend between increasing the number of compound angles and the axial & lateral resolution was similar: na=10 and na=15 showed the lowest resolution in both the lateral & axial direction.

The results of changing the angle between the angular transmissions (dθ), the distance from the transducer to the wire and the voltage are shown in Appendix A.1. In F-mode, the increase of dθ from 0.04 to 0.08 rad resulted in a higher lateral and unchanged axial resolution for all compounding angles. In PI-mode, the lateral resolution also increased when the dθ was set to 0.08 rad, except for na = 5. The axial resolution was also not changed by changing the dθ setting.

The lateral and axial resolution in F- and PI-mode decreased with an increase of voltage. The lateral resolution in F-mode decreased $\sim$0.8 mm between 20 and 50V for all compounding angles, in both dθ=0.04 and 0.08 rad. The axial resolution decreased $\sim$0.3 mm. In PI-mode, the difference in lateral and axial resolution between 20V and 50V was averagely 0.5 mm. The lateral resolution in na=5 showed a larger difference: $\sim$1 mm.

Increasing the distance from the transducer to the wire resulted in a lower lateral resolution in F-mode for all compounding images, it decreased from approximately 2 mm at 2 cm depth to approximately 3 mm at 5.4 cm depth. The axial resolution decreased with approximately 0.2 mm when the depth increased from 2 to 5.4 cm. In PI-mode, the increase of the imaging depth also resulted in a decrease in lateral resolution, except for two outliers at na=5 and na = 10. The axial resolution was not affected by changes in imaging depth.

4.1.2. Localization precision

The locations of the wire reflection found by using four localization methods (i.e. RegionProps, Intensity-Weighted, Gaussian profile, 2D Gaussian surface) are plotted in Figure 4.3a. The locations determined by all methods were distributed in a region of 30 μm axial and 90 μm lateral.

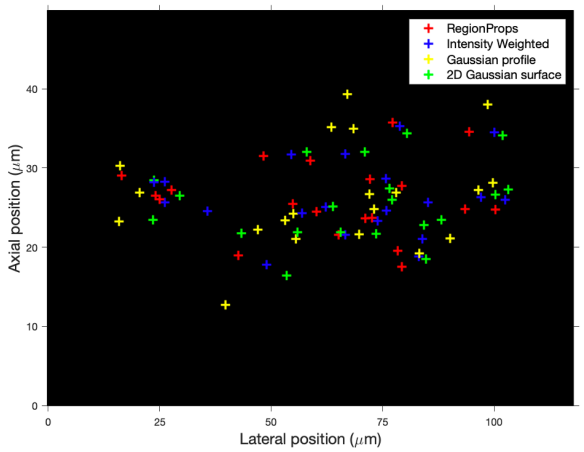

(a) Scatter plot of the locations found by each method.

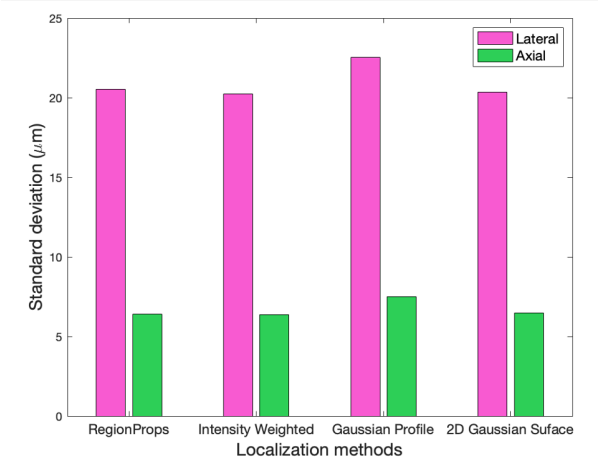

(b) Bar plot of the lateral & axial standard deviation from the locations found by each method

Figure 4.3: The distribution of locations derived with four methods: RegionProps, Intensity-Weighted COM, Gaussian profile fit and 2D Gaussian surface fit. On the scatter plot, the Gaussian profile method showed the widest distribution in axial and lateral direction. On the bar plot, the Gaussian profile was 2 μm larger in the lateral direction and 1 μm larger in axial direction than the other methods. RegionProps, Intensity weighted and 2D Gaussian surface performed similar with a difference of <0.2μm.

Quantification of the distribution by measuring the standard deviation of the data-points showed small differences between the tested methods (Figure 4.3b). The lowest standard deviation was found in the Intensity-Weighted and 3D Gaussian method. Compared to each-other, they differed <2 μm in both the lateral and axial dimension. The localization precision of the imaging system was lateral 20 μm and axial 6 μm according to both the Intensity-Weighted and the 2D Gaussian surface localization method.

4.2. MB detection

During the MB detection experiments, the live reconstructions were monitored for presence of flow. During all acquisitions, it was visually confirmed that the MBs were present in the channel except in the fundamental transmission mode, where the MBs could hardly be recognized from the background. Two images of the maximum intensity projection (MIP) of the frames in fundamental (F) mode and pulse inversion (PI) mode are shown in Figure 4.4. The red frame indicates the region of interest of the channel at a depth of 4 cm, which was used in further experiments. The images acquired in PI-mode clearly showed the location of the channel. In the F-mode, the channel was harder to recognize because of lower contrast with the background.

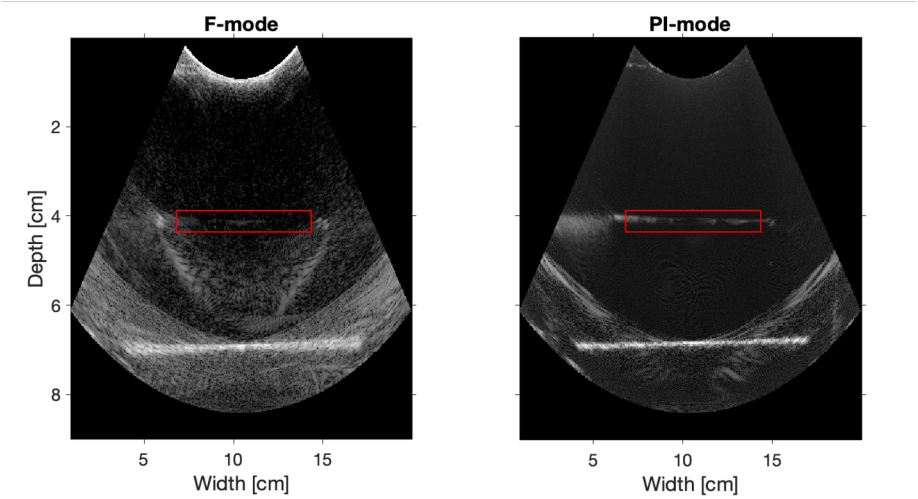

Figure 4.4: The Maximum Intensity Projections of frames acquired in F- and PI- transmission mode during MB flow. Acquisition parameters: fundamental receive mode, 5 compound angles, flow 2 mm/s, 13.7V, no filtering. The region of interest (the channel) used in further experiments is outlined in red. In the F-mode, the channel was less highlighted by the accumulation of the MB signals than in PI-mode.

An example of a MB detection is shown in Figure 4.5. The red circle outlines the MB visible in transmission mode PI at frame 80 using 20 compounding angles, no filtering and the fundamental receive mode.

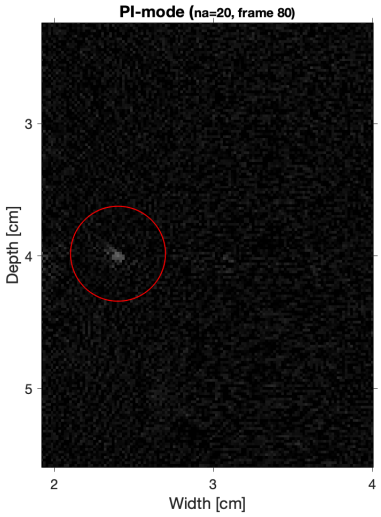

Figure 4.5: A single MB detection in PI transmission-mode, imaging with 20 compounding angles. The circle outlines the MB that was detected at a depth of 4 cm, at a distance ~2 cm from the beginning of the ROI indicated in Figure 4.4.

4.2.1. The effect of number of angle and voltage variation on MB detection

The effect of changing the number of compound angles and variation of the voltage on the MB detection was quantified for the images acquired in PI-mode, with a constant flow of 2 mm/s, no filtering, fundamental receive mode and no induced tissue motion.

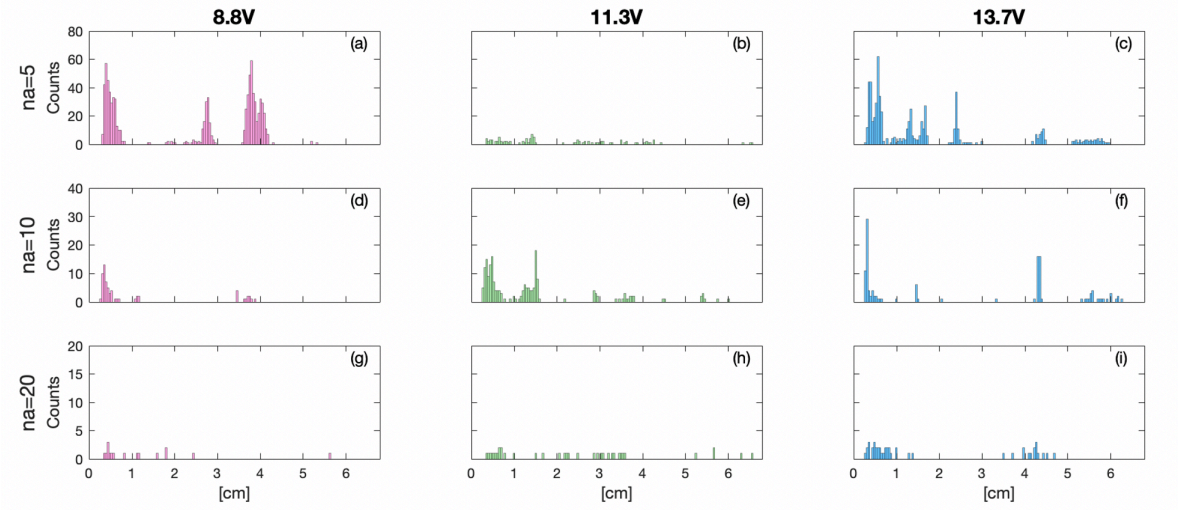

Figure 4.6: Histogram of the number of MBs detected in the channel in PI-transmission mode. The horizontal axes display the dimension of the channel, where 0 cm is the inlet. The vertical axes measure the MB counts in a binsize of 0.4 mm. Each row shows a different set of compound angles (na=5, na=10 and na=20) and each column the voltage (8.8V, 11.3 or 13.7V) used for the acquisition. An increase of number of angles showed a decrease in MB detections. An increase in voltage did not show a direct relation to the number of MB detection. *Note, the total number of frames differed between na=5, na=10 and na=20. The vertical axes are scaled to account for this difference.*

The increase of the number of angles used for coherent compounding resulted in a decrease in MB detections (Figure 4.6). In the na=5 group, approximately half of the frames contained one or more MB detection(s), except for the acquisition at 11.3V (Figure 4.6, b). The number of MB detections decreased in the na=10 and the na=20 group. This applied for all voltages tested.

The increase of the scanning voltage showed different results between the angles. In the na=5 group, the increase from 8.8V tot 11.3V resulted in a strong reduction in MB detections, while at 13.7V the number of MB detection increased again. In the na=10 group, the 11.3V frames show the highest number of MB detections, followed by 13.7V and 8.8V. For na=20, the increase of voltage resulted in an increase of MB detections.

For all acquisitions, more MBs were detected on the inlet side of the channel than on the outlet. For na=5, the ratio of MB detections in the first 3 cm to the last 3 cm, increased with the voltage. This ratio did not apply to na=10 or na=20.

All detected MBs showed a high probability of lying in the channel (Table 4.1). The number of false positive detections was low, except for the acquisition with na=5 and 11.3V.

	8.8V	**11.3V**	**13.7V**
na=5	0%	19%	0%
na=10	0%	0%	0%
na=20	0%	3%	0%

Table 4.1: The fraction of MB detected outside the channel (false positives). All MBs were expected to lie in the channel, except for MBs detected in the na = 5, 11.3V acquisition.

To summarize, an increase in the number of angles used for coherent compounding resulted in a decrease in total MB detections at all voltages tested except at 11.3V. The relation between the voltage and the number of MB detections was different between na=5, na=10 and na=20.

4.2.2. The effect of SVD-filtering or Harmonic receive-mode on MB detection at different flow velocities

To assess the effect of SVD-filtering or the Harmonic receive-mode on the MB detection, images were acquired in PI transmission-mode with 10 compounding angles and a voltage of 11.3V for a duration of 4 sec. Three flow velocities were tested: 1, 2 and 4 mm/s. The live reconstructions of the frames acquired in these settings showed MB flow in the channel for the velocities 2 and 4 mm/s. The presence of MB flow was less clear during acquisition at 1 mm/s.

SVD-filtering resulted in an almost complete disappearance of MB detections for all velocities (Figure 4.7: d, e & f). The Harmonic receive-mode (Figure 4.7: g, h & i) resulted in a sparser MB population than the images corresponding to the fundamental receive-mode (Figure 4.7: a, b & c) at all tested velocities, except at 1 mm/s.

The increase of the flow velocity showed different results between the filtering (none or SVD) and receive (fundamental or harmonic) methods. In the non-filtered data, the increase of flow velocity from 1 mm/s to 2 mm/s resulted in an increase of MB detections (a,b,c). At a flow velocity of 4 mm/s, less MBs were detected than in 1 and 2 mm/s. In the SVD-filtered data, the increase of flow velocity from 1 till 2 till 4 mm/s resulted in more MB detections (d,e,f). In the harmonic receive-mode data this trend was reversed: a higher flow velocity resulted in less MB detections (g,h,i).

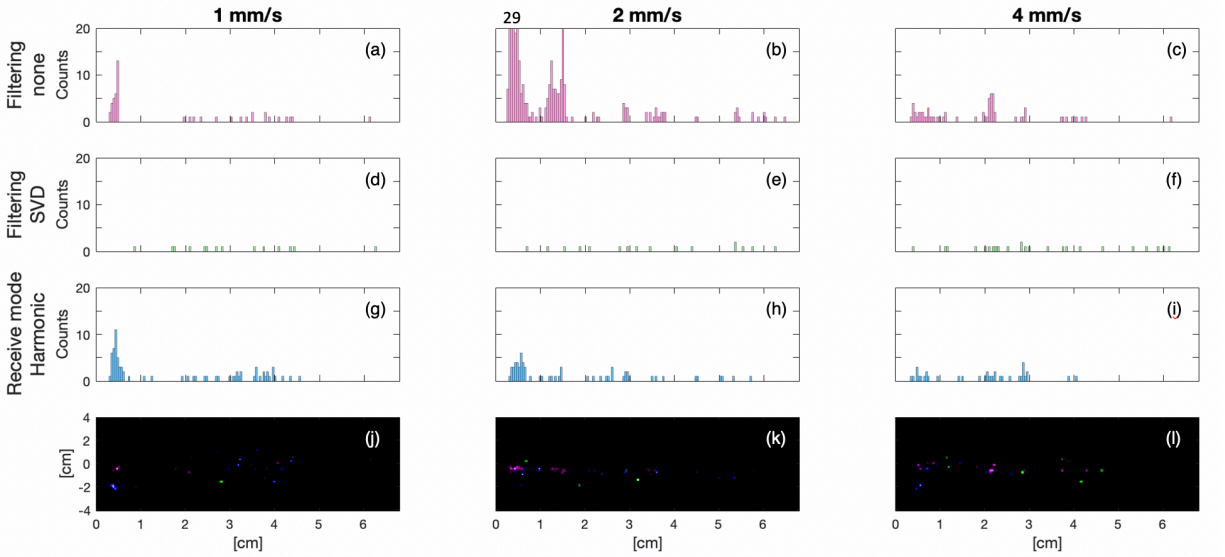

Figure 4.7: Histograms of the number of MBs detected in PI transmission-mode. The first row shows the non-filtered data in the fundamental receive-mode, the second row the SVD-filtered data in the fundamental receive-mode and the third row the non-filtered data in the harmonic receive-mode. Each column shows the flow velocity during acquisition (1, 2 or 4mm/s). The last row shows images of super-localized MBs, colors corresponding to the filtering or receive method. The horizontal axes display the dimension of the channel, where 0 cm is the inlet. The vertical axes of the histograms measure the MB counts in a binsize of 0.4 mm. The vertical axes of the super-localized images display the axial dimension of the channel, where 0 is the estimated center. In the images, the brightness of the dots relates to the probability of finding a MB in that location. SVD-filtering showed an almost complete disappearance of MB detections. Harmonic receiving, showed a decrease in MB detections compared to the fundamental receive-mode, except for flow velocity 1 mm/s. The increase in velocity did not show a direct relation to the number of MB detections in the non-filtered frames. In the SVD-filtered frames, increase of velocity was accompanied by an increase in MB detections. In the harmonic-received frames, this relation was reversed.

Almost all MBs detected in the non-filtered PI data lied in the channel (Table 4.2). SVD-filtering resulted in the highest false positive rate. The total number of MB detections after SVD0filtering increased with flow velocity, while the fraction of false positive values decreased. In the harmonic receive-mode, the total number of MB detections decreased and so did the false positive fraction.

The MBs detected in the non-filtered, SVD-filtered and harmonic receive-mode frames showed different locations (Figure 4.8). At the 1 mm/s flow, the non-filtered and harmonic receive-mode frames showed 4 similar MBs at the inlet side of the channel. On the harmonic receive-mode frames, a dense population of MB detections was located on the first cm outside the channel. No overlap with the SVD-filtering frames was found and the majority (64%, see Table 4.2) was detected outside the channel. At the 2 mm/s flow, the total number of MB detections increased and all lied within the borders of

	1 mm/s	2 mm/s	4 mm/s
No filter	4%	0%	0%
SVD filter	64%	50%	24%
Harmonic	68%	20%	19%

Table 4.2: The fraction of false positive MBs detected. The SVD- and harmonic-received frames resulted in higher false positive MB detections than non-filtered frames. For the SVD-filtered and the harmonic receive-mode images, the false positive fraction decreased with an increase of flow velocity.

the channel. 16 of the 50 MBs detected inside the channel on the harmonic receive-mode frames, overlapped with MBs detected on the non-filtered frames. At this velocity, no overlap in location between the MBs detected in SVD-filtering and the other images was found. At a flow of 4 mm/s, 5 of the 30 MBs detected inside the channel on the harmonic receive-mode frames, overlapped with MBs detected on the non-filtered frames. Again, no overlap with the MBs detected in the SVD-filtered frames was observed.

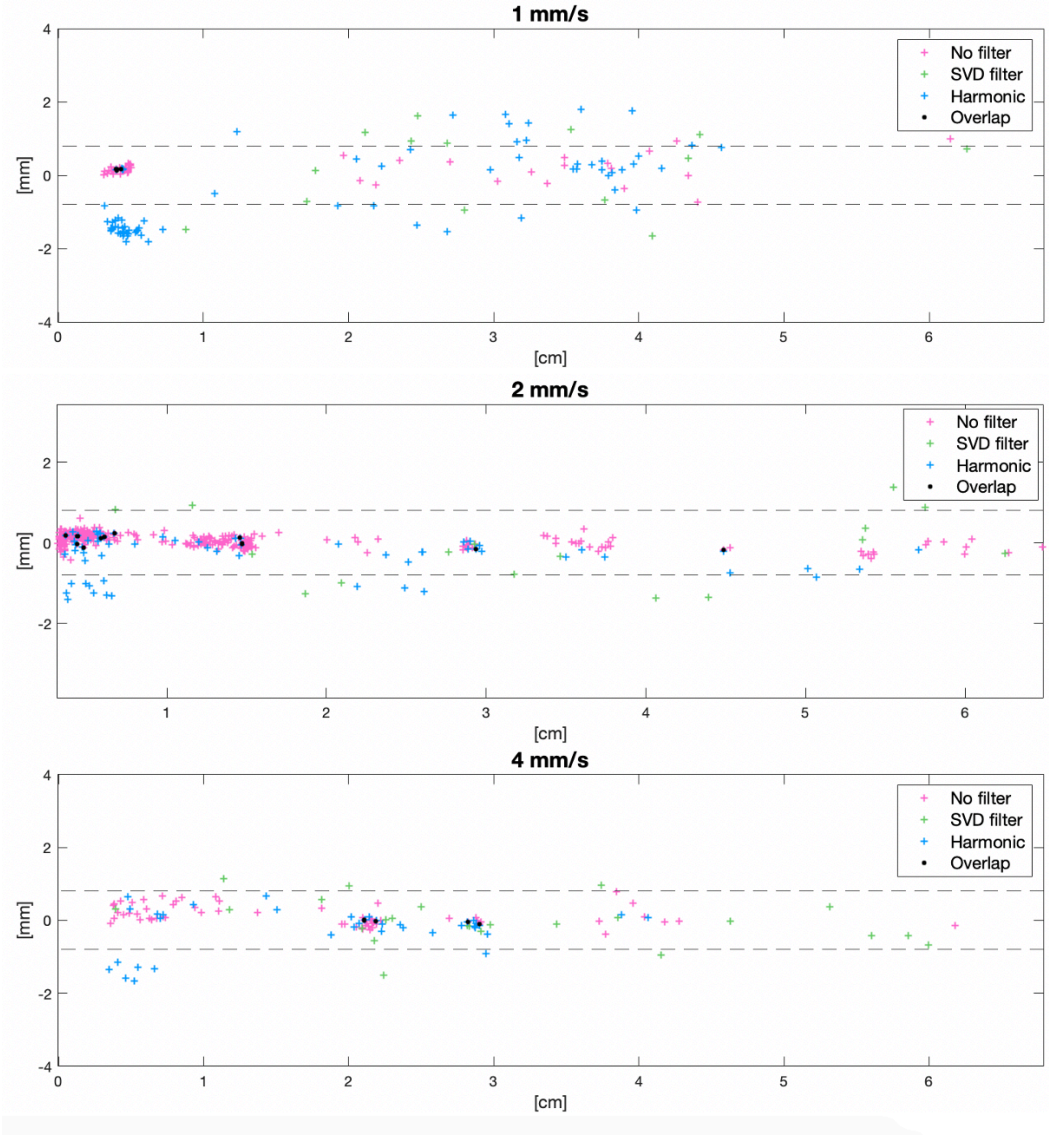

Figure 4.8: Scatter plots of the MB locations found in PI transmission-mode on non-filtered, SVD-filtered and harmonic receive-mode images at flow velocities 1, 2 and 4 mm/s. The dashed lines show the region of the channel, the origin of the plot is the estimated inlet of the channel. Similar MBs were detected at the non-filtered and harmonic receive-mode images for all velocities. The most overlap between No filter and Harmonic in MB detections was at 2 mm/s. No similar MBs were detected in the non-filtered and SVD-filtered frames.

To summarize, the non-filtered fundamental receive-mode frames resulted in the highest true positive MB detections for all tested velocities. SVD-filtering showed a reduction of this value, however the increase of flow velocity was accompanied by an increase in total MB detections and a decrease in the false positive fraction. The harmonic receive mode also reduced the number of true positive MB detections in comparison to the fundamental receive-mode. Here, an increase in flow was accompanied by a decrease in MB detections and a decrease in the false positive fraction.

4.2.3. The effect of transmission mode, receive mode and SVD-filtering on MB detection

The effect of imaging in F or PI transmission-mode, receiving in the harmonic mode and SVD-filtering on the MB detections was assessed in images acquired with 5 compounding angles, with a voltage of 13.7V and a flow of 2 mm/s. During acquisition in F transmission-mode, the live reconstructions of the frames acquired using these settings showed the MBs more clear than using a 10 or 15 compound angles, a lower voltage or a different flow. The acquisition recording time in PI transmission-mode was 4 sec and in F transmission-mode 2 sec.

More MBs were detected in PI-mode than in F-mode (Figure 4.9, a & b). The MBs detected in PI-mode were more distributed over the channel, while in F-mode two large peaks were observed at approximately 0.5 cm and 3.5 cm. MB detection at other locations in the channels were sparse (one or two MBs detected at 3 and 4 cm).

The SVD-filtering of the F transmission-mode frames resulted in a decrease of MB detections from 156 MBs to 92 MBs (Figure 4.9, d). The MBs detected on the SVD-filtering frames were more distributed over the channel and the peaks detected in the non-filtered frames at 0.5 cm and 3.5 cm were flattened out. Transmitting in the F-mode and receiving in the harmonic mode, resulted in a decrease of total MB detections (Figure 4.9, f): 156 MBs in non-filtered frames to 104 MBs in the harmonic receive-mode frames. The peak visible at 0.5 cm in the non-filtered frames was filtered out in the harmonic receive-mode and the peak at 3.5 cm increased (62 detections to 82 detections). The peak shown in the harmonic receive-mode images shifted ~1mm towards the left in comparison to the peak detected in the non-filtered frames.

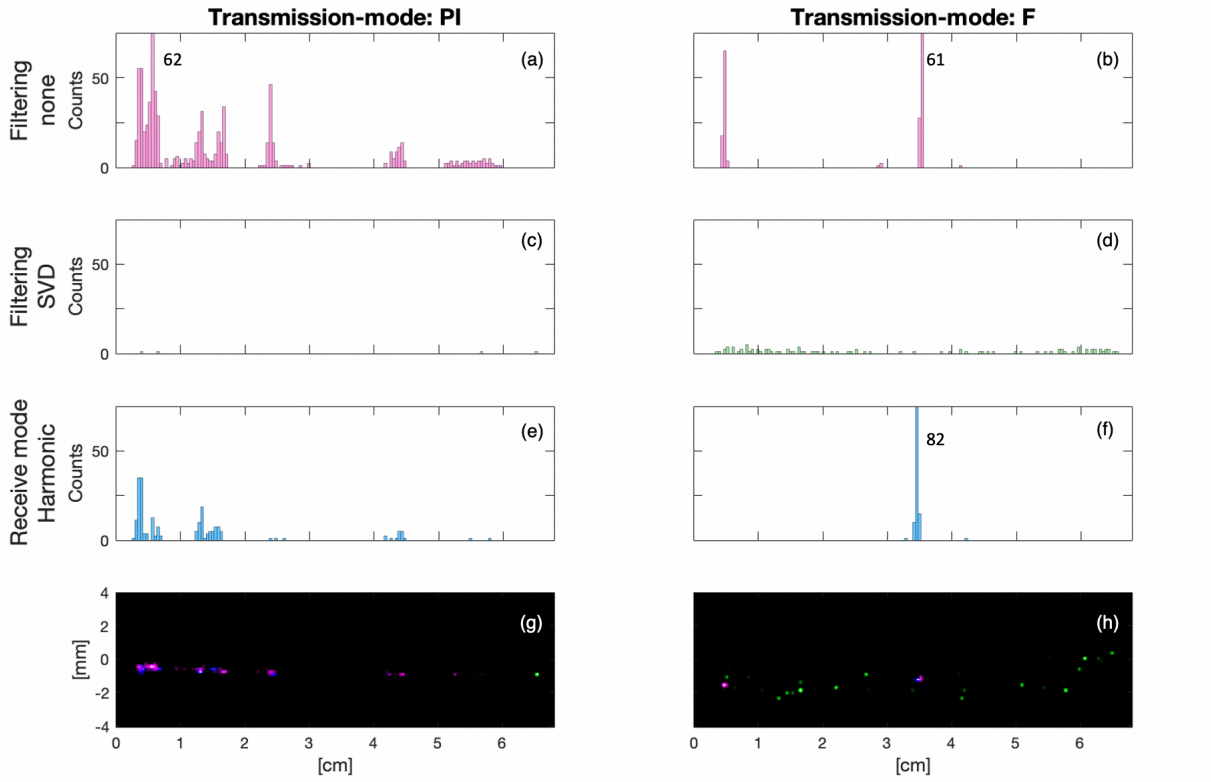

Figure 4.9: Histograms of the number of MBs detected in PI- or F- transmission-mode, with or without SVD-filtering or received in the fundamental or harmonic receive-mode. The first row shows the non-filtered data in the fundamental receive mode, the second row the SVD-filtered data in the fundamental receive mode and the third row the non-filtered data in the harmonic receive mode. Each column shows the transmission mode (PI or F). The last row shows images of super-localized MBs, colored in the method of filtering or receiving. The horizontal axes display the dimension of the channel, where 0 cm is the inlet. The vertical axes of the histograms measure the MB counts in a binsize of 0.4 mm. The vertical axes of the super-localized images display the axial dimension of the channel, where 0 is the estimated center. In the images, the brightness of the dots relates to the probability of finding a MB in that location. In the F transmission-mode, the non-filtered and harmonic receive-mode showed the most MB detections at ~3.5 cm. In the F transmission-mode SVD-filtered frames, the MBs detections were distributed over the channel. In comparison to PI transmission-mode, less MBs were detected in the F-mode frames.

In PI transmission-mode the MBs detected without filtering and in the harmonic receive-mode were all expected to lie inside the channel (Table 4.3). 108 of the 165 detected MBs in the harmonic receive-mode overlapped with the MB detected in the non-filtered PI-mode frames (Figure 4.10, upper). In PI+SVD, 4 MBs were detected from which one lied outside the channel. The locations of the other 3 MBs did not correspond to the the MBs detected in the non-filtered PI-mode frames.

	Transmission mode: PI	**Transmission mode: F**
No filter	0%	44%
SVD filter	25%	66%
Harmonic	1%	0%

Table 4.3: The fraction of false positive MBs detected. The false positive rate was higher in F transmission-mode than in PI transmission-mode. The most false MB detections were made after SVD-filtering for both transmission modes.

In the non-filtered F transmission-mode frames, 44% of the detected MBs lied outside the channel. The fraction increased when the frames were SVD filtered. Most of the MBs detected in these frames lied below the channel (Figure 4.10, lower). The MBs detected on the harmonic frames all lied inside the channel at a distance of ~3.5 cm from the inlet.

The locations of the MBs detected in the non-filtered, SVD-filtered and harmonic receive-mode frames acquired in F transmission-mode did not overlap. The MBs at ~3.5 cm detected in the non-filtered and harmonic receive-mode frames lied approximately 1 mm apart, which was too much to conclude that their location overlapped.

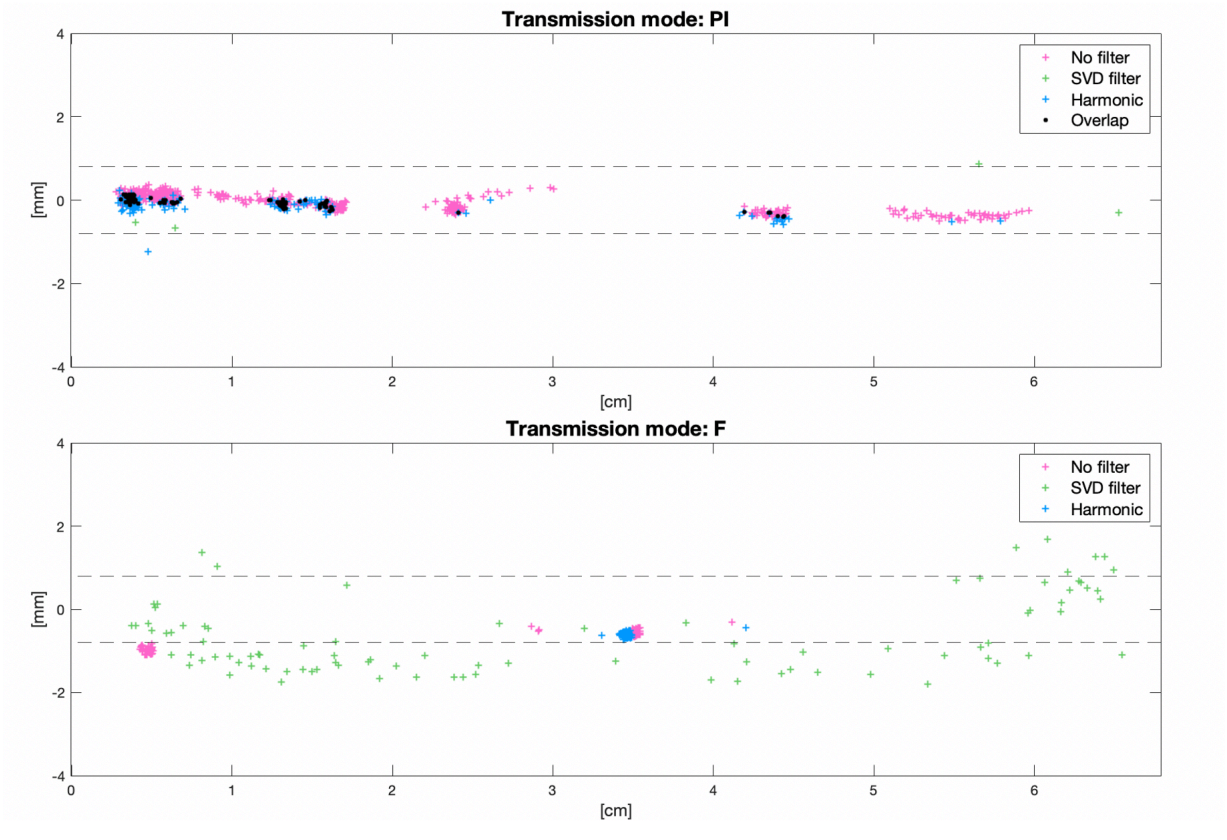

Figure 4.10: Scatter plots of the MB locations found on non-filtered, SVD-filtered and harmonic receive-mode frames acquired in PI- and F-transmission mode. The dashed lines show the estimated region of the channel, the origin of the plot is the estimated inlet of the channel. Similar MBs were detected in non-filtered and harmonic receive-mode PI transmission-mode frames. No similar MB locations were found in F transmission-mode. At 3.5 cm, the harmonic receive-mode frames and the no-filter F-mode frames both showed a high intensity spot which did not overlap. Both transmission modes (PI & F) showed no corresponding MB locations after SVD-filtering.

To summarize, acquisition in the PI transmission-mode resulted in more true positive MB detections than in F-transmission mode. In both transmission modes, SVD-filtering resulted in an almost complete disappearance of MB detections. In the harmonic receive-mode, the total number of MB detections was sparser and, as clearly visible in the F-transmission mode (see Figure 4.10 lower), resulted in a spatial shift of approximately 1 mm.

4.2.4. The effect of SVD-filtering or Harmonic receive-mode on MB detection in moving tissue

To assess the effect of SVD-filtering or the harmonic receive-mode on MB detection in moving tissue, frames were acquired in PI transmission-mode with the following acquisition settings: 10 compounding angles, 13.7V and flow velocity 2 mm/s. The reconstructed frames that were subject to motion, showed high intensity reflections in the channel and the background.

In comparison to the no motion frames, the frames acquired during Induced motions showed twice as much MB detections (Figure 4.11, a vs. b).

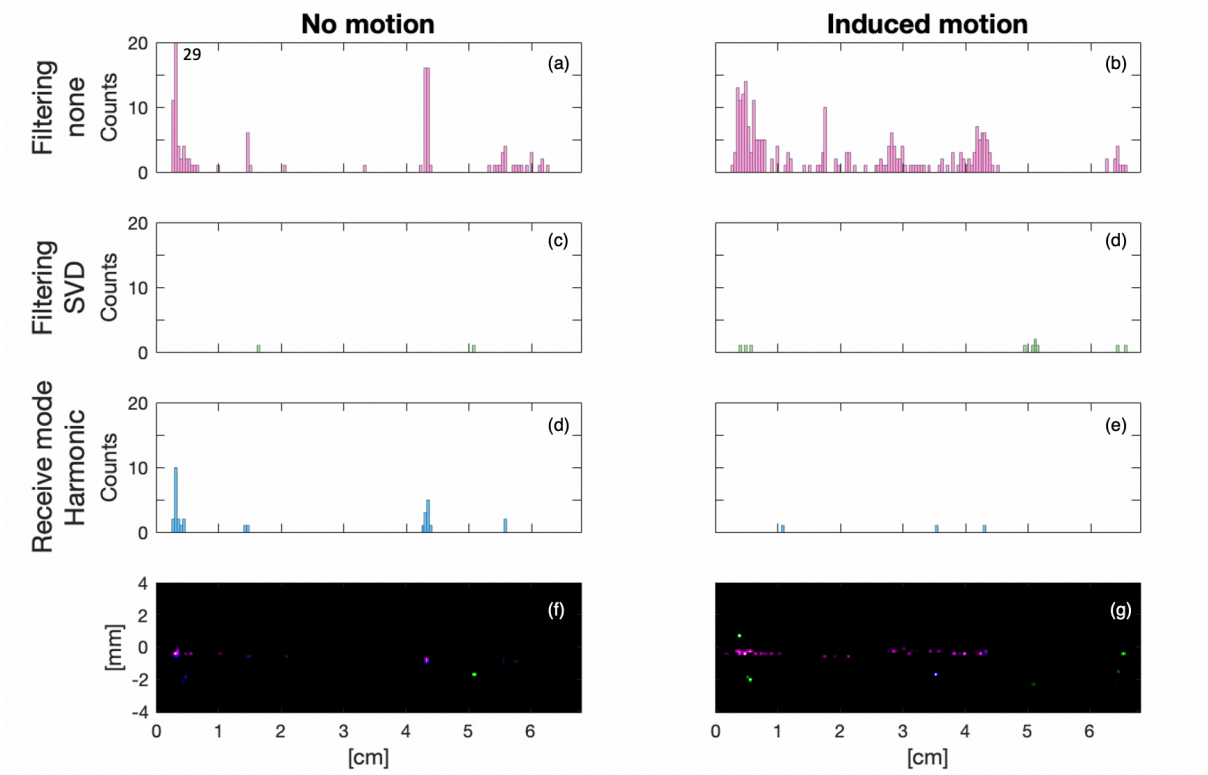

Figure 4.11: Histograms showing the number of MBs detected in PI transmission-mode when tissue motion is induced. The first row shows the non-filtered data in the fundamental receive mode, the second row the SVD-filtered data in the fundamental receive mode and the third row the non-filtered data in the harmonic receive mode. The first column shows the data acquired with no motion. The second column shows the data acquired with motion. The horizontal axes display the dimension of the channel, where 0 cm is the inlet. The vertical axes of the histograms measure the MB counts in a binsize of 0.4 mm. The vertical axes of the super-localized images display the axial dimension of the channel, where 0 is the estimated center. In the images, the brightness of the dots relate to the probability of finding a MB in that location. Induction of motion resulted in more MB detections in the non-filtered MB data. SVD-filtering or receiving in the harmonic mode resulted in an almost complete disappearance of MB detections.

Compared to the stationary case, the detected MBs in the 'Induced motion'-group were more distributed along the channel in the non-filtered frames (Figure 4.11, b). SVD-filtering or the Harmonic receive-mode resulted in a reduction of MBs of more than 95% (Figure 4.11, d & e). This trend was similar in the group where no tissue motion was induced. SVD-filtering or harmonic receive-mode resulted in a reduction in number of MB detections of >95% and 80%, respectively.

For the non-filtered frames acquired during motion, 226 of the 238 MB detections lied inside the channel (Table 4.4). After SVD filtering, 10 MBs were detected from which 1 lied inside the channel. In the harmonic receive-mode, 3 MBs were detected from which 2 were expected to be located in the channel. When tissue motion was induced, a total of 3 MBs were detected on the Harmonic receive-mode frames (Figure 4.12). The 2 MBs that were detected inside the channel overlapped with bubbles detected in the No-filter frames. When no tissue motion was induced, 22 of the 31 MB detected on the Harmonic receive-mode images overlapped.

No overlap in MB detections was found between the non-filtered and SVD-filtered frames acquired with and without motion.

	No motion	Induced motion
No filter	0%	5%
SVD filter	100%	90%
Harmonic	6%	33%

Table 4.4: The fraction of false positive MBs detected. The MBs detected after SVD filtering all (except 1 when motion was induced) lied outside the channel. 1 of the 3 detected MBs on the harmonic receive-mode frames was expected to be located outside the channel.

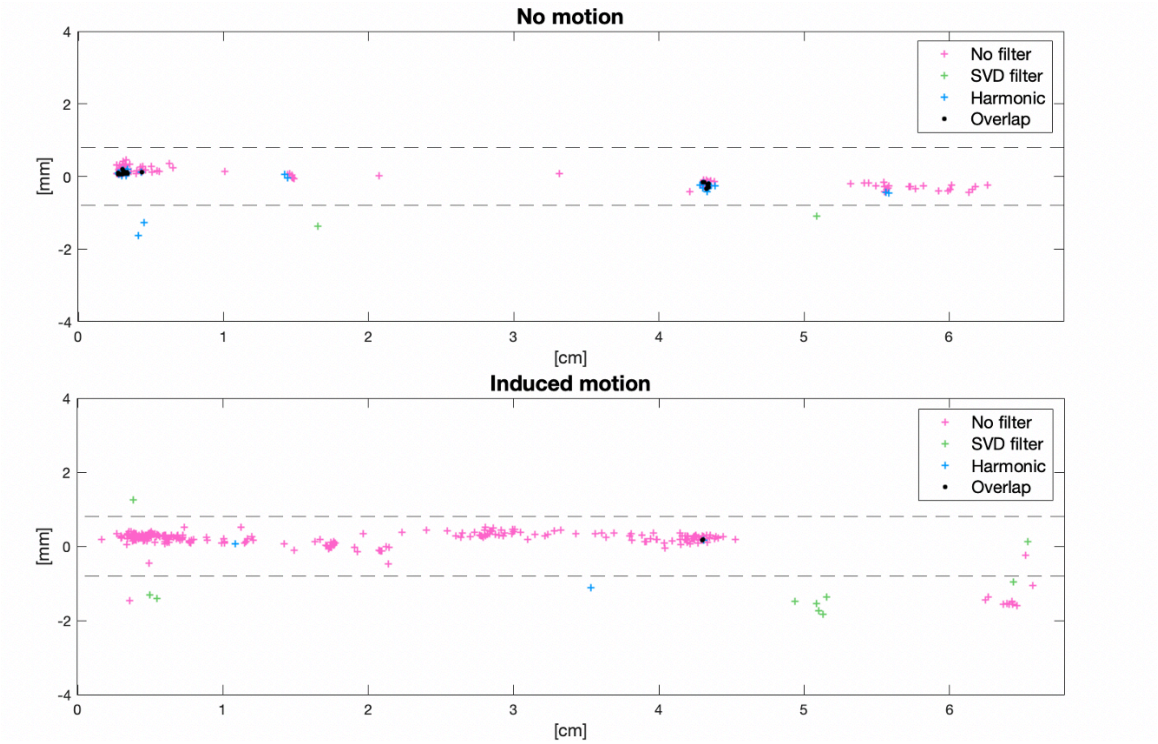

Figure 4.12: Scatter plots of the MB locations detected on non-filtered, SVD-filtered and harmonic receive-mode data acquired in PI transmission-mode with and without induced motion. The dashed lines show the estimated region of the channel, the origin is the estimated inlet of the channel. On the Harmonic receive-mode frames with motion, 3 MBs were detected from which 2 overlap with the non-filtered frames. The SVD-filtered frames resulted in 100% and 90% false MB detections for no motion and induced motion, respectively. No overlap with the non-filtered frames was found.

To summarize, the induction of tissue motion during PI acquisition resulted in a higher number of MB detections in non-filtered PI mode, than when no motion was induced. Application of SVD-filtering or the Harmonic receive-mode resulted in an almost complete loss of MB signals when tissue motion was induced.

5

Discussion

The scope of this project was to determine the effect of pulse inversion and SVD- or harmonic filtering on the number of microbubble detections in ultrasound localization microscopy in slow flow. This search started with a characterization of the ultrasound system in terms of resolution, which was needed as an input for the MB detection algorithm. The results of these experiments are discussed in Section 5.1. The results of the MB detection experiments in which the effect of number of compound angles, volt, flow velocity, transmission mode, receive mode, motion and filtering was evaluated, are discussed in Section 5.2.

5.1. Discussion US characterization

The resolution of the imaging system was assessed by placing a copper wire in a water-container and measuring the full-width-half-maximum of the point spread function of this wire reflection. All experiments were performed in the fundamental receive-mode. Transmission in F-mode showed that an increase of the number of compounding angles from 5 to 20, resulted in a increase of $\sim$1mm in lateral resolution. The axial resolution showed a small (<0.2 mm) decrease. Transmission in PI-mode showed a less clear in- or decrease in the lateral and axial resolution. The na=10 and na=15 measurements resulted in a lower resolution than na=5 and na=20 for both directions.

The trend we observed for the lateral resolution in the F-mode is in correspondence with previous studies [27, 48]. These studies showed that the lateral resolution in coherent compound imaging depends on the maximum transmit angle. A larger maximum transmit angle results in a higher lateral resolution. In our experiment, the difference between the transmitted angles (dθ) was set to 0.04 rad (2°), which means that the largest transmit angle is found in na=20 (23°). The dependency of the lateral resolution on maximum transmit angle is further supported by the results shown in Appendix A.1. When we increased the difference between the angles from 0.04 to 0.08 rad, the maximum transmit angle doubled (23° to 46°). The lateral resolution in F-mode was higher for all voltages, depths and number of angles tested for $d\theta = 0.08$ rad than for $d\theta = 0.04$ rad. In PI-mode, the lateral resolution was also higher at $d\theta = 0.08$ rad for all voltages, depths and number of angles tested. Exceptions were found in na=5 at depth 4 cm, na=10 at depth 5.4 cm and at na=20 at depth 5.4 cm.

If the resolution of the image only depends on the maximum transmit angles and not on the number of angles used, we could reason that using a lower number of transmit angles at a larger dθ would result in the same resolution at a higher frame rate. However, the increase of the angle interval (dθ) introduces grating lobes which interfere with the main lobe [14]. If the angle interval is smaller, the grating lobes are located further away from the main lobe so less disturbance of the image quality occurs. In order to assess the contribution of grating lobes in future research, the beam patterns at the different angle intervals should be evaluated.

On average, imaging in the F-mode showed a lateral resolution of approximately 2.5 mm and an axial resolution of 1 mm. In the PI-mode these findings were slightly smaller: 2 mm lateral and 0.8 mm axial. This can be explained by the fact that in PI-mode, the linear (background) signals are suppressed by the summation of the two transmitted pulses [11]. The PI-signal thus contains higher frequency signals

which improve the axial & lateral resolution.

In general, the PI-signal only contains the non-linear acoustic responses of the medium. In our experiment, these non-linearities could have been generated by two other mechanisms than the non-linear propagation of the scattered signal and therefore could have disturbed the signal. The first is the non-linearity of the Verasonics system: the transmitted wave did not only contain the fundamental frequency but also higher-harmonic frequencies which were reflected by the tissue and the wire. A second option is that the in- and output of the transmitted signal are not linear because the received signal is 'clipped'. When imaging at high voltages, the reflections of the strong reflective copper wire could have exceeded the amplitude range of the system. In that case, the incoming signals were cut-off at a threshold value which results in the production of higher harmonics in the frequency domain. These higher-harmonics disturb the PI-signal, which could explain the variations in the measured lateral and axial resolution in the PI-mode images.

The measurements of the lateral resolution in F-mode showed a clear increase of distribution when the number of angles increased. Also in PI-mode, the distribution of the data-points in the na=10, na=15 and na=20 was larger than in the na=5 group. A possible explanation is that when imaging with more compounding angles, the acquisition time of the frames increases. Small movements of the setup during the acquisition could have led to small spatial shifts which result in a wider distribution of the measured FWHM.

A final remark about the measurement of the resolution is that, unlike expected, the increase in transmit voltage resulted in lower resolution in both axial and lateral direction (see Appendix A.1). The lateral resolution is known to only depend on the imaging depth, wavelength, width of the transducer and maximum compounding angle [1, 48]. The axial resolution is known to only depend on the pulse length [28]. However, the results showed an increase of resolution when the transmit voltage increased from 20V to 50V. This behaviour could be explained by the occurrence of clipping of the system. Secondly, the high voltage transmissions could have given rise to small vibrations in wire, which could have caused a decrease in axial and lateral resolution.

The same experimental setup was used to determine the localization precision of four methods. The location of the wire reflection was determined in 20 frames and the precision of these position was quantified as the standard deviation. The Gaussian profile method resulted in the lowest precision in both axial and lateral dimension, followed by RegionProps. The Intensity-Weighted COM and 2D Gaussian Surface showed the highest precision with a mutual difference of <2μm in the axial and lateral direction. For the MB detection algorithm, we chose to determine the MB location with the 2D Gaussian surface because this method also included outcomes of the goodness of the fit, such a R^2. This value was also used in the MB detection algorithm to differentiate the potential MBs from noise. The Gaussian profile could also provide this information, however the precision of the method was $\sim$3 μm lower lateral and $\sim$2 μm lower axial.

We determined that the localization precision was approximately 20 μm lateral and 6μm axial. The resolution of the super-resolution image is approximately two times the localization precision. In comparison to the average lateral and axial resolution in F-mode (2.5 mm and 1 mm), ULM could theoretically improve the resolution by a factor $\frac{2.5mm}{2 \cdot 20\mu m} \approx 60$ and $\frac{1mm}{2 \cdot 6\mu m} \approx 80$, respectively. In PI-mode the lateral and axial resolution (2 mm and 0.8 mm) improved by a factor of approximately 50 and 70, respectively. This resolution would be sufficient for imaging most microvasculature.

5.2. Discussion MB detection experiments

The results of the MB detection experiments showed diverse results. The overall objective of the experiments was to test five hypotheses regarding the effect of pulse inversion, SVD-filtering and harmonic receive-mode on the MB detections. The results of the MB detection experiments were categorized in four sub-groups, each addressing a different set of acquisition parameters. The results of each group are discussed below. The discussion closes with some general remarks about the project and recommendations for future research.

5.2.1. Discussion of the effect of number of angle and voltage variation on MB detection

The increase in the number of compound angles resulted in a lower number of MB detections, except for the acquisitions at 11.3V. Here, the na=5 group showed a lower number of MB detections than the frames acquired with na=10 and na=20. This measurement also showed a higher false positive fraction than the na=10 and na=20 in the 11.3V group.

The relation between the number of compound angles and the number of MB detections found in the results is opposite of the hypothesis. Previous research showed that the image contrast improves with 10 dB with when the number of angular plane wave transmissions increases from 1 till 20 [27]. When image contrast is high, the MBs can be better differentiated from the background.

An explanation for the opposite trend between MB detection and compounding angles is that MBs disrupt after being longer exposed to the acoustic field. Zhu et al (2019) showed that if the MBs are exposed to acoustic pressures for a longer period of time, this could lead to their disruption [47]. They showed that at low a mechanical index (0.1), MB disruption is still 23% when the MB is longer than half a second exposed. In that case, the chance of finding an MB is lower in the na=20 group than in the na=5 group. For the MB to be detected in the na=20 group by PI transmission-mode, the MB should be present for 16 ms, while in the na=5 group this is a factor 4 shorter.

A second explanation for the opposite trend between MB detection and compounding angles is that, in the na=5 group, more noise is falsely identified as microbubble. Coherent compounding results in reduced speckle, higher contrast and a reduction in artifacts [27], and therefore less false detections could have been made when imaging with more compound angles. However, this is not supported by the the fraction of false positives, which was 0% for all acquisitions except na=5 at at 11.3V.

A third possible consequence of increasing the number of transmit angles is the occurrence of destructive interference because of the displacement of scatterers between the angle transmissions [14]. In coherent compounding of multiple transmissions, it is assumed that the scatterer minimally displaces between the pulses. However, in MB imaging the MBs continuously flow through the channel which could cause decorrelation of the signals, affecting the image quality. The maximal lateral displacement of the MBs between the angle transmissions without comprimising image quality, can be estimated by the one-quarter rule [30]. This rule states that the maximum displacement of the scatterer should be equal or less than one quarter of the interrogation window, in our case the lateral resolution (LR). We can derive the following relation:

$$v_{max} = \frac{LR}{4 \cdot N \cdot PRP}, \tag{5.1}$$

in which N is the number of transmissions per frame and PRP the pulse repetition period. If we consider the 'worst-case-scenario': PI transmission-mode (finest lateral resolution and double pulse) and 20 transmission angles, the maximal displacement of the scatterer is ∼30 mm/s. It is thus not likely that displacement at the flow velocities tested in our MB detection experiments affected the image quality. This theoretical approach was confirmed by the reconstructed frames, where no interference patterns occurred (see Figure 4.5).

The increase of scanning voltage resulted in different results between the groups of angles. It is known from literature that the increase of transmit power results in more scattering of the MBs shortly before they burst [20]. The increase of MB detections in the frames acquired with 20 compounding angles when the voltage increased, can be explained by the the fact that the MBs scatter more strongly at higher acoustic amplitudes. However, this observation was not supported by the acquisition in the na=10 and na=5 group.

What stands out in all acquisitions is that the number of MBs detected was higher on the left side of the channel than on the right side. This difference can possibly be caused by the disruption of MBs.

As discussed before, MB disruption is higher at higher acoustic amplitudes and longer exposure to the acoustic field [20, 47]. However, this is not supported by our results because the ratio of number of MBs detections on the inlet side (0-3 cm) to the number of MBs detection on the outlet side (3-6 cm) did not increase with voltage. A second explanation for the discrepancy between the number of MB detections left and right is the misalignment of the transducer on the channel.

5.2.2. Discussion of the effect of SVD-filtering or Harmonic receive-mode on MB detection at different flow velocities

The second experiment examined the effects of SVD-filtering or the Harmonic receive-mode on MB detections in PI transmission-mode at different flow velocities. At all tested velocities, the SVD resulted in almost complete disappearance of the MB detections. The few MBs that were detected showed relative high false positive rates which makes the detections presumably false.

SVD-filtering differentiates the tissue and MB signal components based on the change in spatial coherence, which is assumed to be more incoherent in the MB component because of their displacement in flow [45]. Our results showed that SVD is not successful at discriminating the MBs, perhaps because of insufficient displacement. It is plausible that the tissue movement during the acquisition lied in the same range as the the MBs. Therefore, the difference in spatial coherence energy of the slowly moving MBs and the tissue was too small to make a separation.

The results showed that with increasing flow velocity, the number of detected MBs increased and the number of false-positives decreased for the SVD-filtered images, suggesting that SVD filtering performs better at higher velocities. When MBs displace more over time, the spatial coherence energy decreases [13]. Then, the signal corresponding to the MBs is classified in a higher rank after SVD. The difference between the rank from the tissue signal components and the MB signal components increases, which benefits their differentiation.

In the harmonic receive-mode, the MB population in the channel became sparser in comparison to the complete receive-mode at all velocities, except at 1 mm/s. At this velocity, the number of MB detections increased but 68% of these detections were expected to lie outside the channel. It is possible that during acquisition, the small movement of tissue introduced phase shifts which were not cancelled out by pulse-inversion. Therefore, the PI transmission-mode received in the fundamental receive-mode could have contained flash artifacts which were falsely detected as MBs by the MB detection algorithm. After restricting the frequency band of the received signal to the harmonic receive-mode, the flash artifacts were filtered out which resulted in a sparser MB detection. However, the opposite can also be true if we consider that the MBs scatter in the fundamental frequency. The displacement between the consecutive frames could have resulted in a phase shift which was preserved in PI, but filtered out after after applying the harmonic frequency cutoff of 4.8 MHz.

5.2.3. Discussion of the effect of transmission mode, receive mode and SVD-filtering on MB detection

The results of the third experiment showed that imaging using a pulse-inversion pulsing-scheme results in a higher number of MB detections than images acquired in the fundamental pulsing-scheme. Both the visual monitoring of the live reconstructions during acquisition and the quantification of the MB detections indicated a higher contrast between the MBs and the background in PI-mode than in F-mode.

Previous research by Desailly at al. (2017) compared F-mode SVD-filtering to power-modulated pulse-inversion (PMPI) Doppler and PMPI nonlinear imaging [16]. They showed that, when probe speed is low (0.8 mm/s) or high (2 mm/s) linear SVD and nonlinear PMPI result in similar contrast-to-tissue ratio, higher than Doppler PMPI at a flow speed of 2 mm/s. Their experience implies that linear SVD is valuable, even with a moving surrounding at low MB flow speeds. Therefore, it was expected that SVD-filtering of the fundamental transmission-mode in our experiments would result in satisfying MB detections. However, our results showed that SVD-filtering in F-mode resulted in 92 detections with a false positive fraction of 66% and non-filtered PI-mode (nonlinear image) resulted in 616 with a false positive fraction of 0%. This discrepancy is possibly explained by the difference between the setup used by Desailly et al. (2017) and our setup. They measured the contrast in a larger (5 mm) vessel at a similar MB concentration, causing each frame to contain approximately thirteen times as much MBs than in our experiment. The chance of a MB signal standing out in each the frame is higher,

which benefits the SVD filtering.

Another possible explanation is that we did not successfully select the ranks for SVD. Our ranks selection was based on the guideline described by Yu & Lovstakken [46], which selects the SVD cutoff rank based on the successive singular values. The first energy decrease between two consecutive eigenvalues that is less than 1%, is chosen as cutoff rank. In future research, the effect of using different cutoff ranks on MB detection in both F- and PI-mode should be evaluated.

The results of imaging in the F transmission-mode and the Harmonic receive-mode showed a decrease in the total number of MB detections: 156 in the fundamental receive-mode to 104 in the harmonic receive-mode. However, the detections at the peak at ∼3.5 cm increased (61 to 82) in the harmonic receive-mode. This peak was slightly (∼1mm) shifted to the left on the harmonic imaging. In the quest of finding an explanation for this spatial shift, we came across the following: The high pass filtering was performed with a second-order Cheby II filter using the Matlab asymmetric function 'filter'. The RF data of the unfiltered and the filtered data showed a shift of the peaks: resulting in a displacement of the envelope of the signal. This could explain the 1 mm shift between the non-filtered data and the harmonic receive-mode data. This could also explain why the locations of the MB detections in PI (transmission-mode) in the fundamental and the harmonic receive-mode did not fully overlap. In future research, it is recommended to use a symmetric filtering operation such as the function 'filtfilt' in Matlab. This filter approaches the RF data from front-to-back and back-to-front, resulting in symmetric high pass filtered RF data.

5.2.4. Discussion of the effect of SVD-filtering or Harmonic receive-mode on MB detection in moving tissue

High intensity reflections were visible on the PI-mode frames recorded when tissue motion was induced. Unlike expected, these frames showed twice as much MB detections than the frames where no motion was induced. This could be explained by the following: In the Harmonic receive-mode the fundamental frequencies were filtered out which resulted in the suppression of flash artifacts. Where flash artifacts were falsely identified as MBs in the complete receive mode PI frames, they were suppressed in the harmonic mode which resulted in a decrease of MB detections.

SVD-filtering in moving tissue also resulted in poor MB detection. From the detected MBs, 1 MB was expected to lie in the channel. The other 9 MBs lied approximately 1 mm below the channel. Logically, the motion of the phantom also resulted in a displacement of the channel. If the channel displaced 1 mm down, the false positive fraction of SVD would go to 0 %. However, it is not likely that SVD in moving tissue improved MB detection, because the SVD-filtering in not-moving tissue also shows poor detection rates. Since this is not in line with previous research, such as the work by Desailly et al. [16], it is possible that these findings are related to mistakes made in the implementation of SVD. As discussed above (Section 5.2.3), a mistake in the selection of the cutoff ranks could have been made.

5.3. General remarks & recommendations

Finally, some general discussion topics about the project and recommendations for future research.
First, the super-localization algorithm did not always provide a robust tool for differentiation between MBs, noise and tissue. As shown in the final experiment in which tissue motion was induced, the number of MB detections increased. These detections could as well have been artifacts caused by the tissue motion, however the MB detection algorithm could not differentiate this. Tightening of the intensity thresholds used in the MB detection algorithm would result in less noise pollution, with the consequence of losing MBs as well [43]. This inconsistency in the MB detection algorithm could have biased the outcomes in this project. For future research, it is recommended to use more sophisticated image analysis software to detect the MBs and make a better differentiation between the MBs and noise. For example, a simple method could be to trace the MBs between consecutive frames, like described by Errico et al. [18]. If a single scattering event is not also present in a consecutive frame, this is probably noise and can be excluded from further analysis. More advanced methods such as deep-learning based techniques can also be valuable to optimize MB detection, as recently proven by Sloun et al. [41].

Secondly, the maximal recording time of the high-frame-rate saving was limited by Verasonics storage capacity. The maximum size of the RF buffer on the Verasonics is 524288 samples. This limited the number of acquisitions per superframe to 240 (if the data is sampled at four times the sampling

frequency) at a maximal imaging depth of 11 cm. The maximal number of superframes was found to be 25. This introduced a limitation to the recording time. During this project, the PRP is set to 400 μs which resulted in recording times of 2 sec in F-mode and 4 sec in PI-mode. This setting was chosen to enlarge the chance that a MB was detected on the frame. However, as a result the frame rate decreased to values outside the range of ultrafast ultrasound (below 1 kHz). In the future, it would be convenient to design a smarter sequence of storing the RF data, for example by monitoring if the received data contains signals coming from MBs. This would require a MB detection algorithm which recognizes the MBs on the RF-data rather than on the reconstructed-intensity data. Additionally, a larger number of recorded imaging frames also allows tighter setting of the intensity thresholds used in the MB detection algorithm because the consequence of losing MB signals is less, when the total dataset contains more frames.

A third remark is made about the setup used in this project. The flow phantom was made with solely agar, which is a low scattering material. Also, the channel embedded in the agar gel was wall-less. Such favorable conditions are unimaginable in tissue. Heterogeneities in the tissue surrounding the channel generally cause reflection of the US signal which lowers the contrast. A sequel to this research project could be to test the performance of PI in a phantom which contains high reflective objects. Additionally, it should be tested whether PI-images still lead to MB detections if the channel has a diameter of 10 μm, the range of the smallest vessels in the human body.

The last remark concerns the transducer and center frequency used in this project. The C5-2 has a bandwidth of 1-5 MHz and a center frequency of 3.2 MHz which is above the frequency in which the strongest MB response is expected [22]. The work by Gorce et al. shows that the large SoneVue MBs peak at 1.5-2 MHz and contribute 80% to the returning signal [22]. When imaging at a transmit frequency of 3.2 MHz, this means that the second harmonic has a frequency of 6.4 MHz which does not lie in the bandwidth of the transducer. Furthermore, 6.4 MHz is also the Nyquist frequency of the chosen Verasonics sampling frequency (12.8 MHz). Therefore it is recommended that in future research, an evaluation of the frequency content of the signals is done. Based on this evaluation, the frequencies used in transmission and high pass filtering can be customized. A good starting point for the transmit frequency would be to adjust it to the range of 1.5-2 MHz. Then, the second harmonic (3 - 4 MHz) lies well within the bandwidth of the C5-2.

Finally, future research should explore different background suppression methods. At first, slow-time high pass filtering like used in conventional Doppler imaging can be explored. Additionally, the effect of other contrast-specific detection schemes such as amplitude modulation (AM) and amplitude modulated pulse inversion (AMPI) on the MB detection can be evaluated. The work by Eckersley et al. (2005) showed that AMPI results in a enhanced level of MB signal in comparison to AM and PI [17]. This improvement is explained by the preservation of both the second and the third order harmonic signal in AMPI. These higher order terms appear in the frequency band of the lower order terms [29], which means they can be detected by the C5-2. Another option is to use more advanced clutter filtering methods such a deep learning based SVD. Recent work by Solomon et al. (2020) showed that this technique outperforms regular SVD, also when MB signal is sparse [34].

6

Conclusion

The quality of super-resolution images is largely dependent of the ability to detect MBs. In good conditions (stationary, strong scatterer), we deduced that ULM improves the axial & lateral resolution of the US images with an average factor of 75. This results in a resolution in the range of tens of micrometers, which is sufficient for imaging most microvasculature. However, sparse MB concentrations flowing at low velocities are less ideal conditions and detection is complicated by poor differentiation between MB and tissue signals. The goal of this project was to evaluate the effect of pulse inversion, SVD-filtering and the harmonic receive-mode on the number of MB detections in ultrasound localization microscopy in these conditions.

The results of this project show that a higher number of MBs is detected in PI-mode (616 MB detections, 0% false positive) than in F-mode (156 MB detections, 44 % false positive). For the voltages used in this study, the increase of the number of compounding angles led to a decrease in MB detections. No direct relation between these voltages and the MB detections was found.

Unlike expected, the number of true positive MB detections in PI transmission-mode is lower in the harmonic receive-mode than in the fundamental receive-mode, for all velocities tested. The false positive fraction was, especially in the 1 mm/s, relatively high compared to the fundamental receive-mode (68% vs. 4 %). This could be explained by the spatial shift caused by the asymmetry of the fast-time frequency filter. Overall, the total number of MB detections decreased in the harmonic receive mode because of the suppression of flash artefacts. These decreases were 46 to 24, 307 to 51 and 65 to 30 for 1, 2 and 4 mm/s, respectively. In the fundamental transmission-mode, the harmonic receive-mode resulted in a higher true positive MB detection rate: 102 true positive MB detections in fundamental receive-mode and 104 true positive MB detections in harmonic receive-mode.

The fourth hypothesis tested was whether SVD-filtering would result in better MB detection in the F & PI transmission-mode. The results in this project show that SVD does not work for the low velocities (1, 2 & 4 mm/s). Only 5, 8 and 19 true positive MB detections were found for 1, 2 & 4 mm/s in PI transmission-mode, respectively. In fundamental transmission-mode, SVD-filtering resulted in 31 true positive detections, which was 50 true positive detections lower than the non-filtered frames.

Finally, none of the tissue suppression approaches in this project results in reliable MB detections in moving tissue. The induction of tissue motion resulted in more true positive MB detections in the non-filtered PI transmission-mode frames, than without motion (124 and 226, respectively). This increase could be due to the introduction of flash artifact because of strong motion. Almost all MB detections disappeared after SVD-filtering or restricting the frequency band to the harmonic receive-mode, where the true positive MB detections were 1 and 2, respectively.

To summarize, MB detection in slow flow is complicated by the presence of reflective tissue. Our study shows that PI transmission-mode outperforms F transmission-mode. SVD-filtering in both modes results in almost complete disappearance of MB detections, possibly because of incorrect rank selection. Filtering of the frequency band to the harmonic receive-mode contributes to the suppression of flash artifacts, however further research at acquisition settings better suited for receiving harmonic frequencies is required. A good starting point would be to transmit more in the range of the resonance frequency of the large MBs (1.5-2 MHz) which contribute 80% to the returning signal [22].

Bibliography

[1] Z. Alomari, S. Harput, S. Hyder, and S. Freear. The effect of the transducer parameters on spatial resolution in plane-wave imaging. pages 1–4, 2015. doi: 10.1109/ULTSYM.2015.0547.

[2] J. C. Bamber and C. R. Hill. Ultrasonic attenuation and propagation speed in mammalian tissues as a function of temperature. *Ultrasound in Medicine and Biology*, 5(2):149–157, 1979. ISSN 03015629. doi: 10.1016/0301-5629(79)90083-8. URL https://www.sciencedirect.com/science/article/pii/0301562979900838.

[3] Eric Betzig, George H. Patterson, Rachid Sougrat, O. Wolf Lindwasser, Scott Olenych, Juan S. Bonifacino, Michael W. Davidson, Jennifer Lippincott-Schwartz, and Harald F. Hess. Imaging intracellular fluorescent proteins at nanometer resolution. *Science*, 313(5793):1642–1645, 2006. ISSN 0036-8075. doi: 10.1126/science.1127344. URL https://science.sciencemag.org/content/313/5793/1642.

[4] J. Brown, K. Christensen-Jeffries, S. Harput, C. Dunsby, M. X. Tang, and R. J. Eckersley. Investigation of microbubble detection methods for super-resolution imaging of microvasculature. In *2017 IEEE International Ultrasonics Symposium (IUS)*, pages 1–4, 2017. doi: 10.1109/ULTSYM.2017.8092177.

[5] K. Christensen-Jeffries, R. J. Browning, M. Tang, C. Dunsby, and R. J. Eckersley. In vivo acoustic super-resolution and super-resolved velocity mapping using microbubbles. *IEEE Transactions on Medical Imaging*, 34(2):433–440, 2015. doi: 10.1109/TMI.2014.2359650.

[6] Kirsten Christensen-Jeffries, Olivier Couture, Paul A. Dayton, Yonina C. Eldar, Kullervo Hynynen, Fabian Kiessling, Meaghan O'Reilly, Gianmarco F. Pinton, Georg Schmitz, Meng-Xing Tang, Mickael Tanter, and Ruud J.G. van Sloun. Super-resolution ultrasound imaging. *Ultrasound in Medicine Biology*, 46(4):865 – 891, 2020. ISSN 0301-5629. doi: https://doi.org/10.1016/j.ultrasmedbio.2019.11.013. URL http://www.sciencedirect.com/science/article/pii/S0301562919315959.

[7] K.M. Christensen-Jeffries. *Super-resolution ultrasound imaging with microbubbles*. PhD thesis, King's College London, 2017.

[8] O. Couture, B. Besson, G. Montaldo, M. Fink, and M. Tanter. Microbubble ultrasound super-localization imaging (musli). *2011 IEEE International Ultrasonics Symposium*, pages 1285–1287, 2011.

[9] O. Couture, M. Fink, and M. Tanter. Ultrasound contrast plane wave imaging. *IEEE Transactions on Ultrasonics, Ferroelectrics, and Frequency Control*, 59(12):2676–2683, 2012. doi: 10.1109/TUFFC.2012.2508.

[10] O. Couture, M. Tanter, and M. Fink. Method and device for ultrasound imaging, Patent Cooperation Treaty PCT/FR2011/052810, 2010.

[11] Nico De Jong, Peter J.A. Frinking, Ayache Bouakaz, and Folkert J. Ten Cate. Detection procedures of ultrasound contrast agents. *Ultrasonics*, 38(1):87–92, 2000. ISSN 0041624X. doi: 10.1016/S0041-624X(99)00071-2.

[12] B. Delannoy, R. Torguet, C. Bruneel, E. Bridoux, J. M. Rouvaen, and H. Lasota. Acoustical image reconstruction in parallel-processing analog electronic systems. *Journal of Applied Physics*, 50 (5):3153–3159, 1979. ISSN 00218979. doi: 10.1063/1.326397. URL https://doi.org/10.1063/1.326397.

[13] C. Demené, T. Deffieux, M. Pernot, B. Osmanski, V. Biran, J. Gennisson, L. Sieu, A. Bergel, S. Franqui, J. Correas, I. Cohen, O. Baud, and M. Tanter. Spatiotemporal clutter filtering of ultrafast ultrasound data highly increases doppler and fultrasound sensitivity. *IEEE Transactions on Medical Imaging*, 34(11):2271–2285, 2015. doi: 10.1109/TMI.2015.2428634.

[14] B. Denarie, T. A. Tangen, I. K. Ekroll, N. Rolim, H. Torp, T. Bjåstad, and L. Lovstakken. Coherent plane wave compounding for very high frame rate ultrasonography of rapidly moving targets. *IEEE Transactions on Medical Imaging*, 32(7):1265–1276, 2013. doi: 10.1109/TMI.2013.2255310.

[15] Y. Desailly, A.M. Tissier, J.M. Correas, F. Wintzenrieth, M. Tanter, and O. Couture. Contrast enhanced ultrasound by real-time spatiotemporal filtering of ultrafast images. *Physics in medicine and biology*, 62(1):31–42, 2017. doi: 10.1088/1361-6560/62/1/31.

[16] Yann Desailly, Juliette Pierre, Olivier Couture, and Mickael Tanter. Resolution limits of ultrafast ultrasound localization microscopy. *Physics in Medicine and Biology*, 60(22):8723–8740, oct 2015. ISSN 13616560. doi: 10.1088/0031-9155/60/22/8723. URL https://doi.org/10.1088/0031-9155/60/22/8723.

[17] R. J. Eckersley, C. T. Chin, and P. N. Burns. Optimising phase and amplitude modulation schemes for imaging microbubble contrast agents at low acoustic power. *Ultrasound Med Biol*, 31(2):213–9, 2005. 0301-5629 (Print) Journal Article Research Support, Non-U.S. Gov't.

[18] Claudia Errico, Juliette Pierre, Sophie Pezet, Yann Desailly, Zsolt Lenkei, Olivier Couture, and Mickael Tanter. Ultrafast ultrasound localization microscopy for deep super-resolution vascular imaging. *Nature*, 527(7579):499–502, 2015. ISSN 14764687. doi: 10.1038/nature16066. URL https://doi.org/10.1038/nature16066.

[19] Judah Folkman. Angiogenesis. *Annual Review of Medicine*, 57(1):1–18, jan 2006. ISSN 00664219. doi: 10.1146/annurev.med.57.121304.131306. URL https://doi.org/10.1146/annurev.med.57.121304.131306.

[20] Peter J.A. Frinking, Ayache Bouakaz, Johan Kirkhorn, Folkert J. Ten Cate, and Nico De Jong. Ultrasound contrast imaging: Current and new potential methods. *Ultrasound in Medicine and Biology*, 26(6):965–975, 2000. ISSN 03015629. doi: 10.1016/S0301-5629(00)00229-5. URL https://www.sciencedirect.com/science/article/pii/S0301562900002295.

[21] V. Gibbs, D. Cole, and A. Sassano. *Ultrasound Physics and Technology*. Churchill Livingstone, Elsevier Health Sciences, 2009.

[22] Jean Marie Gorce, Marcel Arditi, and Michel Schneider. Influence of bubble size distribution on the echogenicity of ultrasound contrast agents: A study of sonovue(TM). *Investigative Radiology*, 35(11):661–671, 2000. ISSN 00209996. doi: 10.1097/00004424-200011000-00003. URL https://journals.lww.com/investigativeradiology/Fulltext/2000/11000/Influence{_}of{_}Bubble{_}Size{_}Distribution{_}on{_}the.3.aspx.

[23] C. Hu, G. Jeng, Y. Wang, P. Li, and M. Li. Improved plane-wave high frame rate imaging using retrospective transmit focusing and filter-derived coherence-index weighting. In *2010 IEEE International Ultrasonics Symposium*, pages 1916–1919, 2010. doi: 10.1109/ULTSYM.2010.5935716.

[24] Jian-yu Lu. Reducing clutter noise in fast ultrasound imaging with transverse high-pass filtering. In *2013 IEEE International Ultrasonics Symposium (IUS)*, pages 1244–1247, 2013. doi: 10.1109/ULTSYM.2013.0318.

[25] A. P. Kadi and T. Loupas. On the performance of regression and step-initialized iir clutter filters for color doppler systems in diagnostic medical ultrasound. *IEEE Transactions on Ultrasonics, Ferroelectrics, and Frequency Control*, 42(5):927–937, 1995. doi: 10.1109/58.464825.

[26] MATLAB. *version 9.5.0 (R2018b)*. The MathWorks Inc., Natick, Massachusetts, 2019.

[27] G. Montaldo, M. Tanter, J. Bercoff, N. Benech, and M. Fink. Coherent plane-wave compounding for very high frame rate ultrasonography and transient elastography. *IEEE Transactions on Ultrasonics, Ferroelectrics, and Frequency Control*, 56(3):489–506, 2009. doi: 10.1109/TUFFC.2009.1067.

[28] Alexander Ng and Justiaan Swanevelder. Resolution in ultrasound imaging. *Continuing Education in Anaesthesia Critical Care Pain*, 11(5):186–192, 08 2011. ISSN 1743-1816. doi: 10.1093/bjaceaccp/mkr030. URL https://doi.org/10.1093/bjaceaccp/mkr030.

[29] P. J. Phillips. Contrast pulse sequences (cps): imaging nonlinear microbubbles. In *2001 IEEE Ultrasonics Symposium. Proceedings. An International Symposium (Cat. No.01CH37263)*, volume 2, pages 1739–1745 vol.2, 2001. doi: 10.1109/ULTSYM.2001.992057.

[30] M. Raffel, C. E. Willert, F. Scarano, C. J. Kähler, S. T. Wereley, and J. Kompenhans. *Particle Image Velocimetry*. Springer International Publishing, Springer Nature, 2018.

[31] L. Sandrin, S. Catheline, M. Tanter, X. Hennequin, and M. Fink. Time-resolved pulsed elastography with ultrafast ultrasonic imaging. *Ultrasonic Imaging*, 21(4):259–272, oct 1999. ISSN 01617346. doi: 10.1177/016173469902100402. URL https://doi.org/10.1177/016173469902100402.

[32] Ricardo Santamaría, María González-Álvarez, Raquel Delgado, Sergio Esteban, and Alicia G. Arroyo. Remodeling of the Microvasculature: May the Blood Flow Be With You. *Frontiers in Physiology*, 11:1256, 2020. ISSN 1664042X. doi: 10.3389/fphys.2020.586852. URL https://www.frontiersin.org/article/10.3389/fphys.2020.586852.

[33] D. H. Simpson, Chien Ting Chin, and P. N. Burns. Pulse inversion doppler: a new method for detecting nonlinear echoes from microbubble contrast agents. *IEEE Transactions on Ultrasonics, Ferroelectrics, and Frequency Control*, 46(2):372–382, 1999. doi: 10.1109/58.753026.

[34] O. Solomon, R. Cohen, Y. Zhang, Y. Yang, Q. He, J. Luo, R. J. G. van Sloun, and Y. C. Eldar. Deep unfolded robust pca with application to clutter suppression in ultrasound. *IEEE Transactions on Medical Imaging*, 39(4):1051–1063, 2020. doi: 10.1109/TMI.2019.2941271.

[35] Brian Starkoff. Ultrasound physical principles in today's technology. *Australasian Journal of Ultrasound in Medicine*, 17(1):4–10, feb 2014. ISSN 1836-6864. doi: 10.1002/j.2205-0140.2014.tb00086.x. URL https://pubmed.ncbi.nlm.nih.gov/28191202https://www.ncbi.nlm.nih.gov/pmc/articles/PMC5024924/.

[36] Thomas L. Szabo. Wave Scattering and Imaging. In Thomas L Szabo, editor, *Diagnostic Ultrasound Imaging: Inside Out*, pages 257–294. Academic Press, Boston, second edition edition, 2014. ISBN 978-0-12-396487-8. doi: 10.1016/b978-0-12-396487-8.00008-2. URL https://www.sciencedirect.com/science/article/pii/B9780123964878000082.

[37] Masayuki Tanabe, Takuya Yamamura, Kan Okubo, and Norio Tagaw. Tissue Harmonic Imaging with Coded Excitation. In Takuya Yamamura, editor, *Ultrasound Imaging*, page Ch. 6. IntechOpen, Rijeka, 2011. doi: 10.5772/15850. URL https://doi.org/10.5772/15850.

[38] Meng Xing Tang, Naohisa Kamiyama, and Robert J. Eckersley. Effects of Nonlinear Propagation in Ultrasound Contrast Agent Imaging. *Ultrasound in Medicine and Biology*, 36(3):459–466, 2010. ISSN 03015629. doi: 10.1016/j.ultrasmedbio.2009.11.011. URL https://www.sciencedirect.com/science/article/pii/S0301562909016597.

[39] M. Tanter and M. Fink. Ultrafast imaging in biomedical ultrasound. *IEEE Transactions on Ultrasonics, Ferroelectrics, and Frequency Control*, 61(1):102–119, 2014. doi: 10.1109/TUFFC.2014.2882.

[40] Johan M Thijssen, Gert Weijers, and Chris L de Korte. Objective Performance Testing and Quality Assurance of Medical Ultrasound Equipment. *Ultrasound in Medicine and Biology*, 33(3):460–471, mar 2007. ISSN 0301-5629. doi: 10.1016/j.ultrasmedbio.2006.09.006. URL https://doi.org/10.1016/j.ultrasmedbio.2006.09.006.

[41] R. J. G. van Sloun, O. Solomon, M. Bruce, Z. Z. Khaing, Y. C. Eldar, and M. Mischi. Deep learning for super-resolution vascular ultrasound imaging. In *ICASSP 2019 - 2019 IEEE International Conference on Acoustics, Speech and Signal Processing (ICASSP)*, pages 1055–1059, 2019. doi: 10.1109/ICASSP.2019.8683813.

[42] J. Vangindertael, R. Camacho, W. Sempels, H. Mizuno, P. Dedecker, and K. P.F. Janssen. An introduction to optical super-resolution microscopy for the adventurous biologist. *Methods and Applications in Fluorescence*, 6(2):22003, mar 2018. ISSN 20506120. doi: 10.1088/2050-6120/aaae0c. URL https://doi.org/10.1088/2050-6120/aaae0c.

[43] O.M. Viessman, R. J. Eckersley, K. Christensen-Jeffries, M. X. Tang, and C. Dunsety. Acoustic super-resolution with ultrasound and microbubbles. *Physics in medicine and biology*, 18(58): 6447–6458, 2013. doi: 10.1088/0031-9155/58/18/6447.

[44] J. Voorneveld, S. Engelhard, H. J. Vos, M. M.J. Reijnen, F. Gijsen, M. Versluis, E. Groot Jebbink, N. de Jong, and J. G. Bosch. High frame rate contrast-enhanced ultrasound for velocimetry in the human abdominal aorta. *IEEE transactions on ultrasonics, ferroelectrics and frequency control*, 65(12):2245–2254, December 2018. ISSN 0885-3010. doi: 10.1109/TUFFC.2018.2846416.

[45] R.R. Wildeboer, F. Sammali, R.J.G. van Sloun, H. Wijkstra, and M. Mischi. Optimal blind-source-separation filtering for ultrasound clutter suppression: application to ultrasound localization microscopy and speckle tracking. In *2019 IEEE International Ultrasonics Symposium, IUS 2019*, pages 2060–2063, United States, October 2019. IEEE Computer Society. doi: 10.1109/ULTSYM.2019.8926008. 2019 IEEE International Ultrasonics Symposium, IUS 2019 ; Conference date: 06-10-2019 Through 09-10-2019.

[46] A. C. H. Yu and L. Lovstakken. Eigen-based clutter filter design for ultrasound color flow imaging: a review. *IEEE Transactions on Ultrasonics, Ferroelectrics, and Frequency Control*, 57(5):1096–1111, 2010. doi: 10.1109/TUFFC.2010.1521.

[47] J. Zhu, S. Lin, C. H. Leow, E. M. Rowland, K. Riemer, S. Harput, P. D. Weinberg, and M. X. Tang. High frame rate contrast-enhanced ultrasound imaging for slow lymphatic flow: Influence of ultrasound pressure and flow rate on bubble disruption and image persistence. *Ultrasound in medicine biology*, 45(9):2456–2470, 2019. doi: 10.1016/j.ultrasmedbio.2019.05.016.

[48] R. Øvland. *Coherent plane-ave compounding in medical ultrasound imaging*. Master's thesis, Norwegian University of Science and Technology Trondheim, 2012.

Appendix A

A.1. Results of system PSF measurements

The parameters that are varied in the US characterization experiments and their ranges are summarized in Table A.1.

Parameters	Range
Number of angles	[5, 10, 15, 20]
dθ	[0.04, 0.08] rad
Transmission mode	[Fundamental, Pulse inversion]
Depth	[2, 4, 5.4] cm
Voltage	[20, 30, 40, 50] V

Table A.1: A list of the parameters that are varied to characterize the system in terms of lateral and axial resolution. The left column shows the parameters and the right column the range in which they are varied.

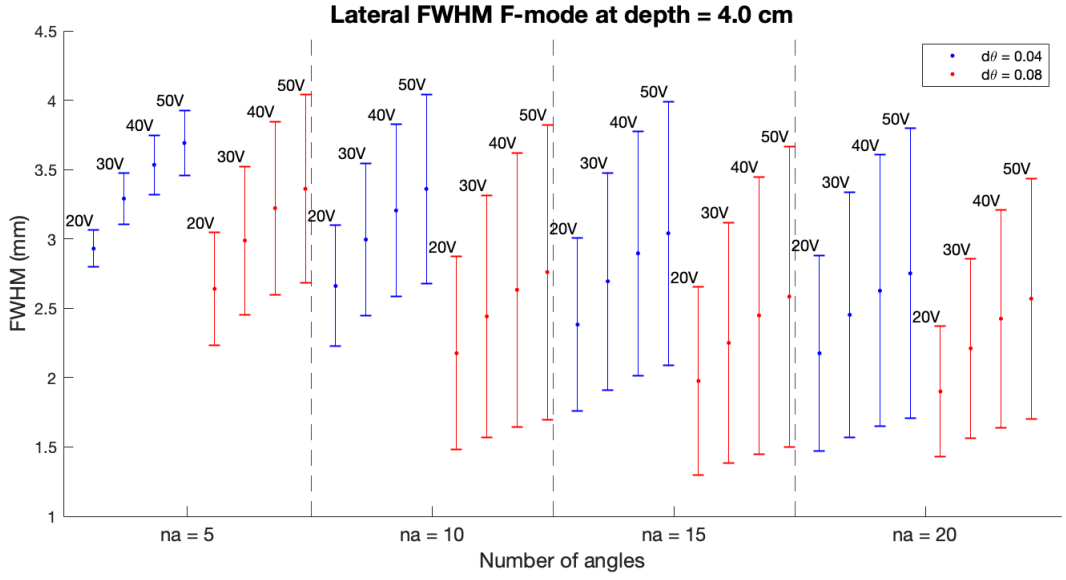

Figure A.1: The lateral FWHM (mm) measured in F-mode at a depth of 4 cm using 5, 10, 15 and 20 compounding angles. The resolution was higher when the number of compounding angles increases. The increase of voltage led to lower resolutions.

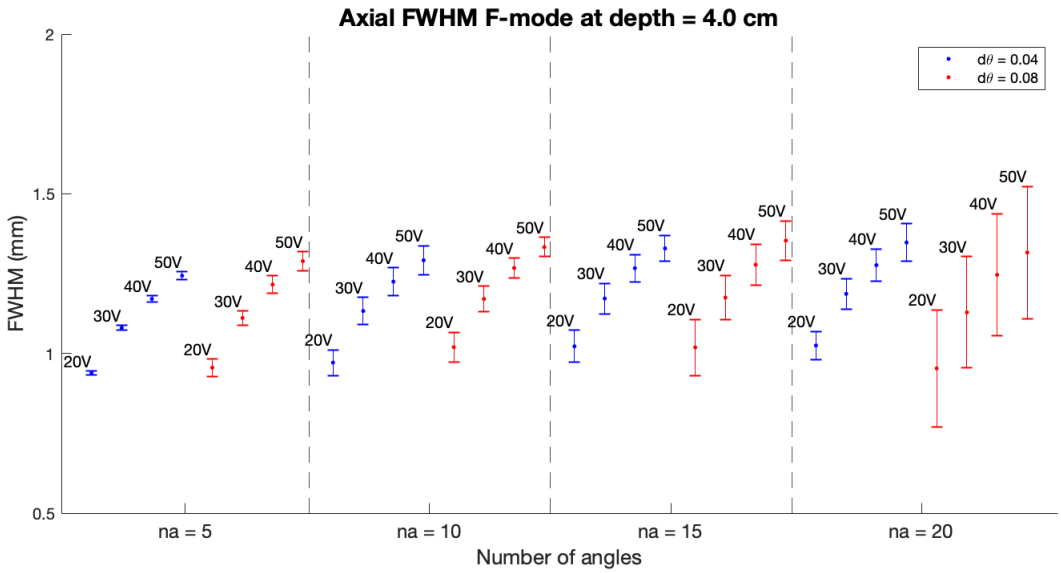

Figure A.2: The axial FWHM (mm) measured in F-mode at different sets of compounding angles. The increase of the number of angles had no effect on the axial resolution. The increase of voltage resulted in a higher FWHM value.

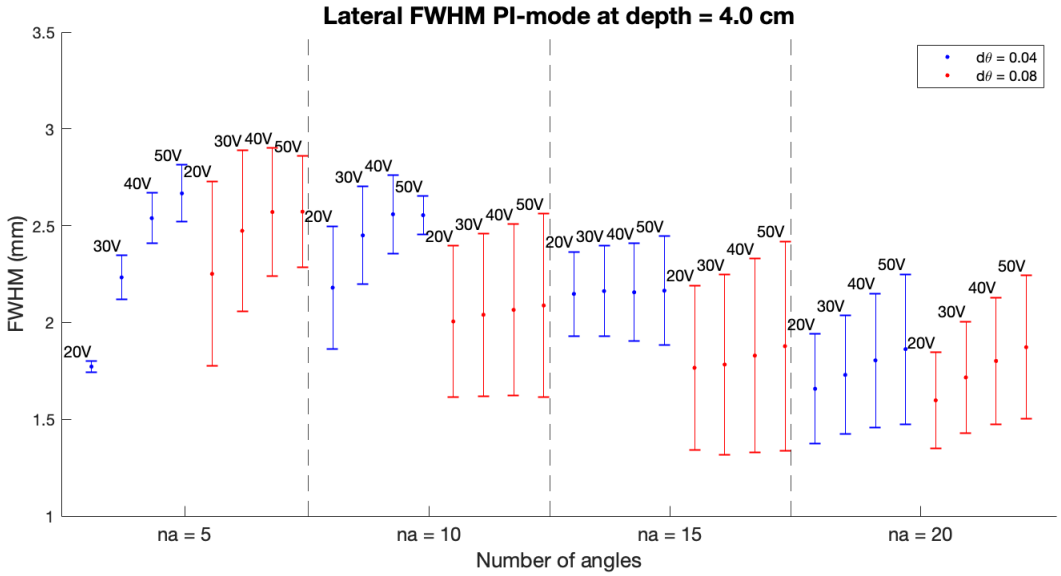

Figure A.3: The lateral FWHM (mm) measured at 4 cm depth in Pulse inversion mode. Like in F-mode, the increase of number of angles led to higher resolutions. The FWHM-value increased with voltage.

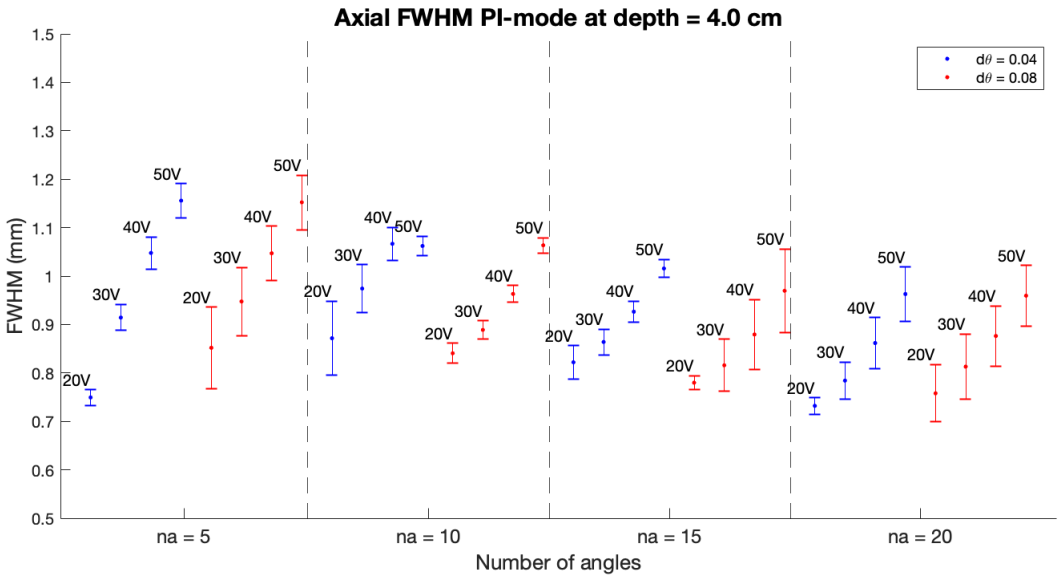

Figure A.4: The axial FWHM (mm) measured at 4 cm depth in Pulse inversion mode. Increasing the number of compounding angles had no effect on the axial resolution. Increasing the voltage did.

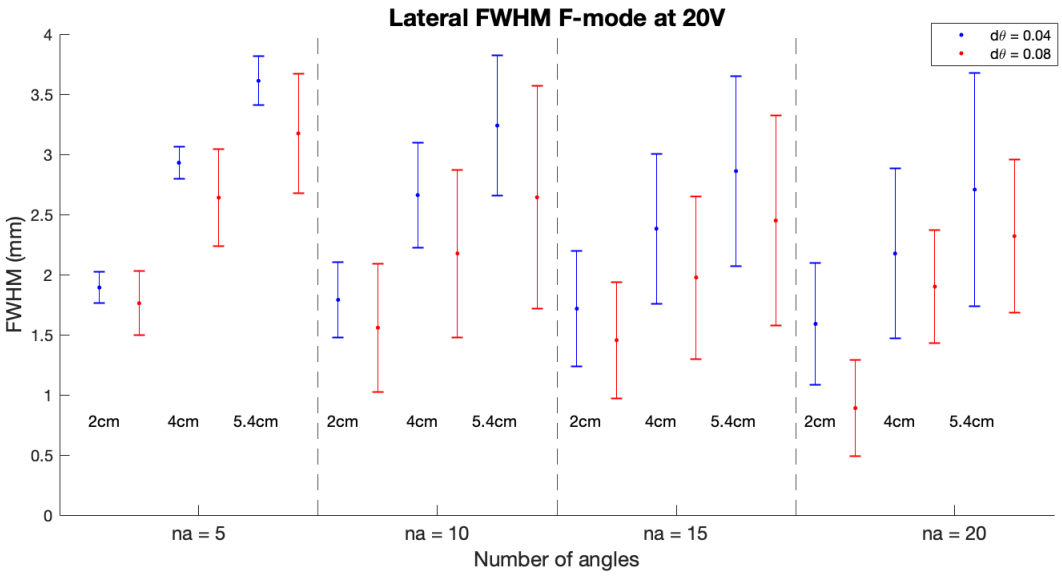

Figure A.5: The lateral FWHM (mm) measured at varying depths. The resolution was lower at larger imaging depths. Increasing the number of angles had no effect.

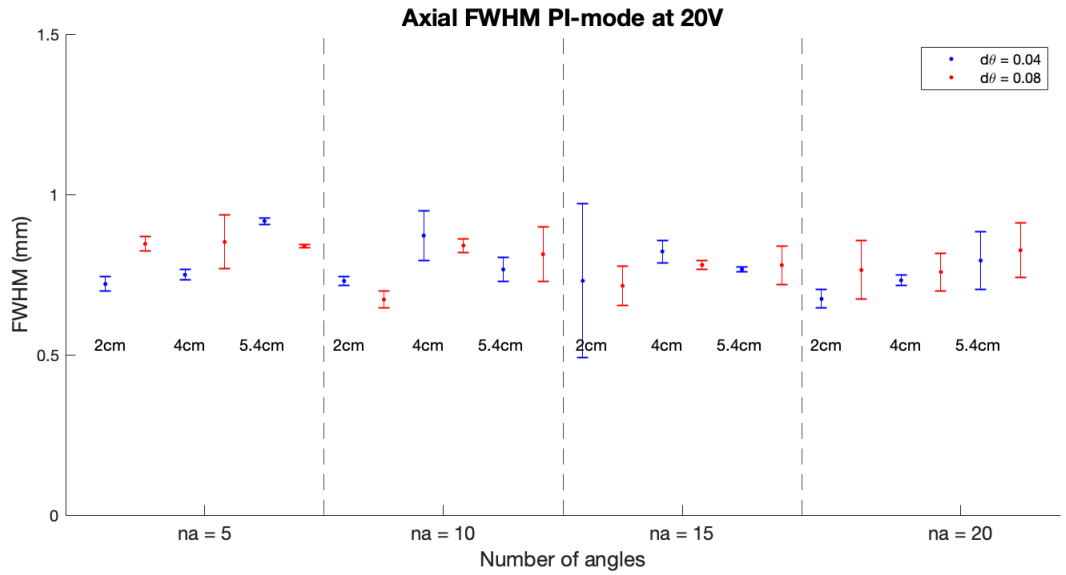

Figure A.6: The axial FWHM (mm) measured at different imaging depths. The resolution only slightly lowerd by increasing the imaging depth. This change was smaller than seen for the lateral resolution.

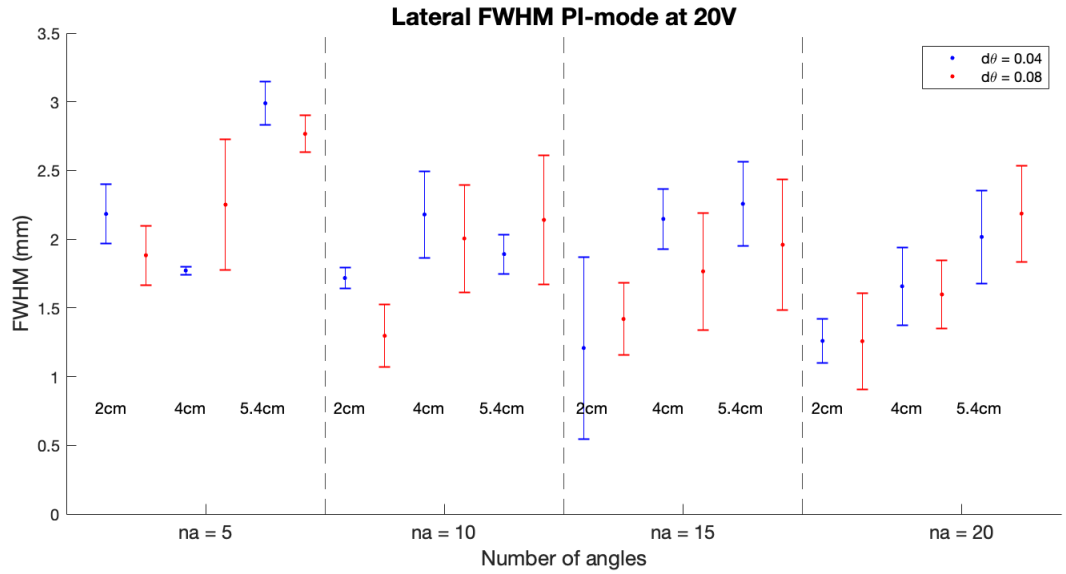

Figure A.7: The lateral FWHM (mm) measured at 4 cm depth in Pulse inversion mode. Higher imaging depths resulted in lower lateral resolution for all compouding angles.

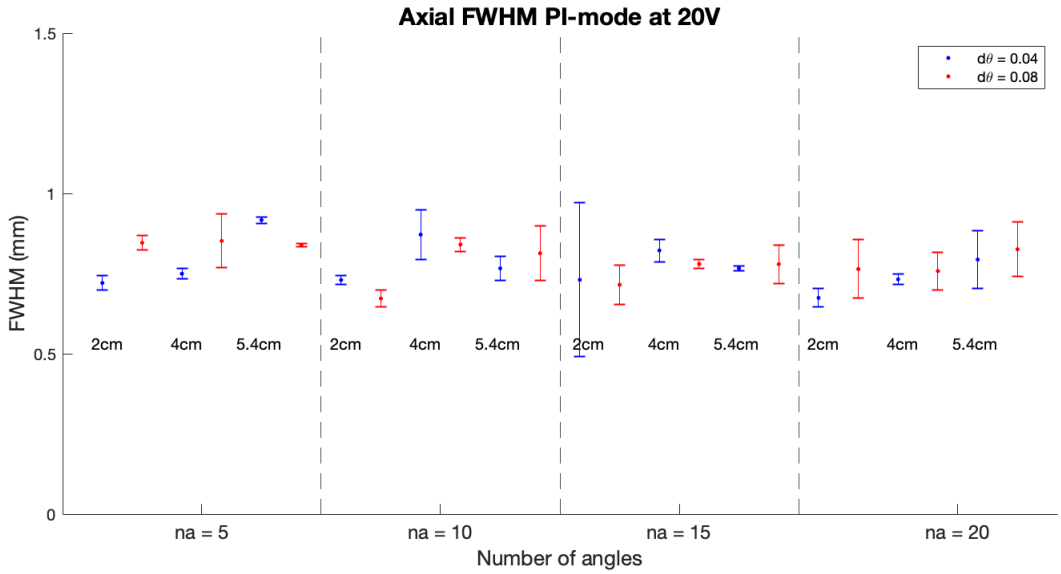

Figure A.8: The axial FWHM (mm) measured at 4 cm depth in Pulse inversion mode. Increasing the imaging depth had no effect on the axial resolution.